Science of the Total Environment 677 (2019) 530–544

Contents lists available at ScienceDirect

Science of the Total Environment

journal homepage: www.elsevier.com/locate/scitotenv

Response of deep aquifers to climate variability

Karem Abdelmohsen [a,b], Mohamed Sultan [a,*], Mohamed Ahmed [c], Himanshu Save [d], Baher Elkaliouby [e], Mustafa Emil [a], Eugene Yan [f], Abotalib Z. Abotalib [a,g], R.V. Krishnamurthy [a], Karim Abdelmalik [e]

[a] Geological and Environmental Sciences, Western Michigan University, Kalamazoo, MI 49008, USA
[b] Geodynamics Department, National Research Institute of Astronomy and Geophysics (NRIAG), Helwan, Cairo 11421, Egypt
[c] Department of Physical and Environmental Sciences, Texas A&M—Corpus Christi, Corpus Christi, TX 78412, USA
[d] Center for Space Research, the University of Texas at Austin, TX 78759-5321, USA
[e] Geology Department, Faculty of Science, Ain Shams University, Cairo 11566, Egypt
[f] Environmental Science Division, Argonne National Laboratory, Argonne, IL 60439, USA
[g] Geology Department, National Authority for Remote Sensing and Space Sciences, Cairo 1564, Egypt

HIGHLIGHTS

- Identification of recharge sources and deep aquifer response to climate variability
- Application of an integrated approach (GRACE, geochemistry, geophysics, and field)
- The Nubian Sandstone Aquifer System (NSAS) in northeast Africa was used as a test area.
- NSAS recharged by infiltration from Lake Nasser and from precipitation in the south
- Rapid groundwater flow from source areas occurs along a network of faults and karst.

GRAPHICAL ABSTRACT

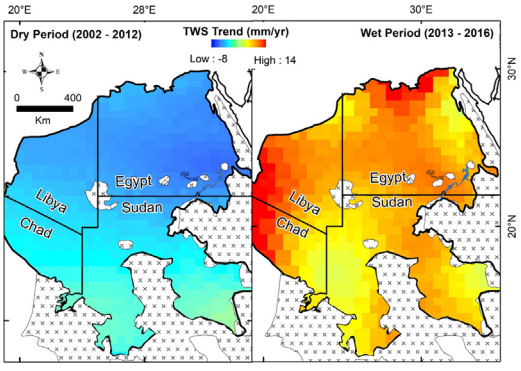

ARTICLE INFO

Article history:
Received 17 February 2019
Received in revised form 19 April 2019
Accepted 20 April 2019
Available online 24 April 2019

Editor: José Virgílio Cruz

Keywords:
Climate variability
Deep aquifer response
Nubian Sandstone Aquifer System
GRACE
Satellite-based precipitation/soil moisture data
Stable isotopes

ABSTRACT

There is a general agreement that deep aquifers experience significant lag time in their response to climatic variations. Analysis of Temporal Gravity Recovery and Climate Experiment (GRACE), Soil Moisture and Ocean Salinity mission (SMOS), satellite altimetry, stable isotopic composition of groundwater, and precipitation and static global geopotential models over the Nubian Sandstone Aquifer System (NSAS) revealed rapid aquifer response to climate variability. Findings include: (1) The recharge areas of the NSAS (Northern Sudan Platform subbasin) witnessed a dry period (2002−2012), where average annual precipitation (AAP) was modest (85 mm) followed by a wet period (2013–2016; AAP: 107 mm), and during both periods the AAP remained negligible (<10 mm) over the northern parts of the NSAS (Dakhla subbasin); (2) the secular trends in terrestrial water storage (TWS) over the Dakhla subbasin were estimated at −3.8 ± 1.3 mm/yr and + 7.8 ± 1 mm/yr for the dry and wet periods, respectively; (3) spatial variations in TWS values and phase are consistent with rapid groundwater flow from the Northern Sudan Platform subbasin and Lake Nasser towards the Dakhla subbasin during the wet period and from the lake during the dry period; and (4) networks of densely fractured and karstified bedrocks provide preferential pathways for groundwater flow. The proposed model is supported by (1) rapid response in groundwater levels in distant wells (>280 km from source areas) and in soil moisture content in areas with shallow (<2 m) groundwater levels to fluctuations in Lake Nasser surface water, and (2) the isotopic composition

* Corresponding author.
E-mail address: mohamed.sultan@wmich.edu (M. Sultan).

https://doi.org/10.1016/j.scitotenv.2019.04.316

(O, H) of groundwater along the preferred pathways, consistent with mixing of enriched (Lake Nasser water or precipitation over Sudan) and depleted (NSAS fossil water) endmembers. Findings provide new insights into the response of large, deep aquifers to climate variability and address the sustainability of the NSAS and similar fossil aquifers worldwide.

1. Introduction

Short-lived climatic variabilities on timescales of years to decades is believed to affect the recharge of shallow (depth to water table [DWT] < 30 m), but not deep, aquifers (Chen et al., 2004; Healy and Cook, 2002). By contrast, the impact of climate change and climatic variabilities on deep aquifer systems spans longer timescales (thousands to tens of thousands of years; Abotalib et al., 2019; Fendorf et al., 2010; Hanson et al., 2006; Sturchio et al., 2004) due to the length of time for precipitation to infiltrate unsaturated soil profiles and underlying shallow aquifers (Dickinson et al., 2014), and for the infiltrated waters to flow from recharge to distant discharge areas (Abotalib et al., 2019). The response of deep aquifers to a recharge signal caused by climatic variations is mainly constrained by the aquifer's properties (e.g., aquifer transmissivity and storativity, thickness of clay interbeds, and the presence of fractures, faults, and karst topography) and depths to groundwater (Geyer et al., 2008; Goode, 1996; Seaton and Burbey, 2005; Walton, 2011). The well-established time-lag response of deep aquifer systems has been recently challenged with reported sub-annual deep aquifer response to short-lived climatic variabilities in the United States (Russo and Lall, 2017) and by the presence of young decadal-aged waters with measurable tritium within deep (>250 m) fossil aquifers (Jasechko et al., 2017). However, the mechanism by which modern precipitation infiltrates and mixes with fossil groundwater in deep aquifers is still poorly understood. In this manuscript, we use data from the Gravity Recovery and Climate Experiment (GRACE) satellite to document a rapid response to short-lived climatic variabilities over a deep, extensive (area: 2×10^6 km^2), fossil aquifer in northeast Africa, the Nubian Sandstone Aquifer System (NSAS) and provide possible mechanisms for the observed rapid response.

The GRACE satellite was launched in 2002 to map the temporal variations in Earth's global gravity field and mean gravity field (Tapley et al., 2004a, 2004b). The variability in the gravity field solutions at the time scales examined by GRACE (i.e., days to years) are largely related to redistribution of mass at, or near, Earth's surface (Wahr et al., 2004). GRACE measures the variability in terrestrial water storage (TWS), which refers to the total water content for all the reservoirs (e.g., groundwater, surface water, snow and ice, soil moisture and permafrost, or wet biomass) in an area. Spherical harmonic (SH) solutions of GRACE gravity data have been used successfully to measure TWS variations over large hydrologic systems (Ahmed et al., 2014, 2016; Ahmed and Abdelmohsen, 2018; Mohamed et al., 2017; Sultan et al., 2013, 2014; Wouters et al., 2014), yet their applications on subbasin scales were hindered by their coarse spatial resolution (>125,000 km^2), leakage problems, and the required complex post-processing steps (Scanlon et al., 2016). Three publicly available GRACE solutions were utilized in this study: the relatively high-resolution (hexagonal tiles ≈120 km at the equator) Release-05 (CSR-RL05M) monthly mass concentration (mascon) solutions (Save et al., 2016) from the Center for Space Research at the University of Texas (UT-CSR; http://www.csr.utexas.edu/grace), the mascon solutions from the Jet Propulsion Laboratory (JPL; ftp://podaac-ftp.jpl.nasa.gov/allData/tellus/L3/mascon/RL05/JPL/CRI/netcdf/) (JPL-RL05M), and the spherical harmonics of the UT-CSR GRACE solution (CSR- RL06SH; Level 2; degree/order: 60; available at: ftp://podaac-ftp.jpl.nasa.gov/allData/grace/L2/CSR/RL06). The mascon solutions are advantageous compared to the spherical harmonics given their higher signal-to-noise ratio, higher spatial resolution, and reduced leakage errors. Moreover, they do not require post processing including de-striping or smoothing filtering or any scaling to compensate for the attenuation of the geophysical signals caused by de-striping (Scanlon et al., 2016; Ahmed and Abdelmohsen, 2018).

The NSAS with its simple hydrologic setting allows straightforward interpretations of the observed temporal variations in GRACE TWS solutions, a situation that does not readily apply to the more complex hydrologic systems worldwide. For example, recharge occurs in the southern sections of the NSAS (Sudan and Chad), where the aquifer crops out and where the average annual precipitation (AAP) could reach up to 1000 mm/yr locally and is minimal to absent in the northern parts (Egypt and Libya) where precipitation is negligible (AAP: <20 mm/yr). Using the NSAS in northeast Africa (Fig. 1), we demonstrate that throughout the investigated period (April 2002 to June 2016), the observed temporal GRACE mass variations were largely controlled by recharge in the south and from Lake Nasser and by the rapid and preferential groundwater flow along complex fracture/fault systems and karst topography. Findings were corroborated by field, geophysical, topographic, and isotopic investigations. We would have not been able to demonstrate these findings if we dealt with more complex systems where precipitation and recharge are occurring across the entire aquifer.

2. Geologic and hydrogeologic settings

The NSAS consists mainly of thick (>3 km) Paleozoic and Mesozoic continental sandstone intercalated with marine Tertiary carbonates, shale, and clay deposited in shallow marine and deltaic settings (Hesse et al., 1987). The aquifer is bound by basement from the east and south, the Devonian bedrock from the west, and by the saltwater-freshwater interface in the north (Sultan et al., 2013). The NSAS is formed of three major subbasins that are separated by basement uplifts. The Uweinat-Aswan uplift separates the Dakhla subbasin (Egypt) from the Northern Sudan Platform subbasin (northern Sudan) to the south, and the Uweinat-Howar uplift separates the latter (Northern Sudan Platform subbasin) from the Kufra subbasin (Libya, northeastern Chad, and northwestern Sudan) to the west (Hesse et al., 1987; Fig. 1). Along segments of these uplifts, the basement crops out or reaches near surface elevations, yet in other segments along the length of the uplifts, the depth to basement increases allowing groundwater flow through these windows (Ahmed et al., 2016). The Kufra subbasin is here subdivided into the Northern Kufra and the Southern Kufra sections that are separated by a threshold AAP line of 20 mm (Fig. 1). Groundwater flow is generally from the southwest to the northeast, and the aquifer is confined north of latitude 25°N but unconfined to the south of it in the Dakhla subbasin (Ball, 1927; Sanford, 1935).

The NSAS is composed of two major hydrological units: the sandstone-dominated Nubian aquifer system (NAS) and the overlying carbonate-dominated post-Nubian aquifer system (PNAS; Bakhbakhi, 2006). The NSAS was largely recharged during previous pluvial periods in the Quaternary by intensification of paleomonsoons (Prell and Kutzbach, 1987; Sarnthein et al., 1981; Yan and Petit-Maire, 1994) or paleowesterlies (Abouelmagd et al., 2014; Sturchio et al., 2004; Sultan et al., 1997). At present, the aquifer is receiving modest local recharge in the southern highlands (e.g., Gebel Darfur in Sudan and Gebel Tibesti in Chad; Fig. 1) where the Nubian Sandstone crops out and where precipitation reaches up to 96 mm/yr.

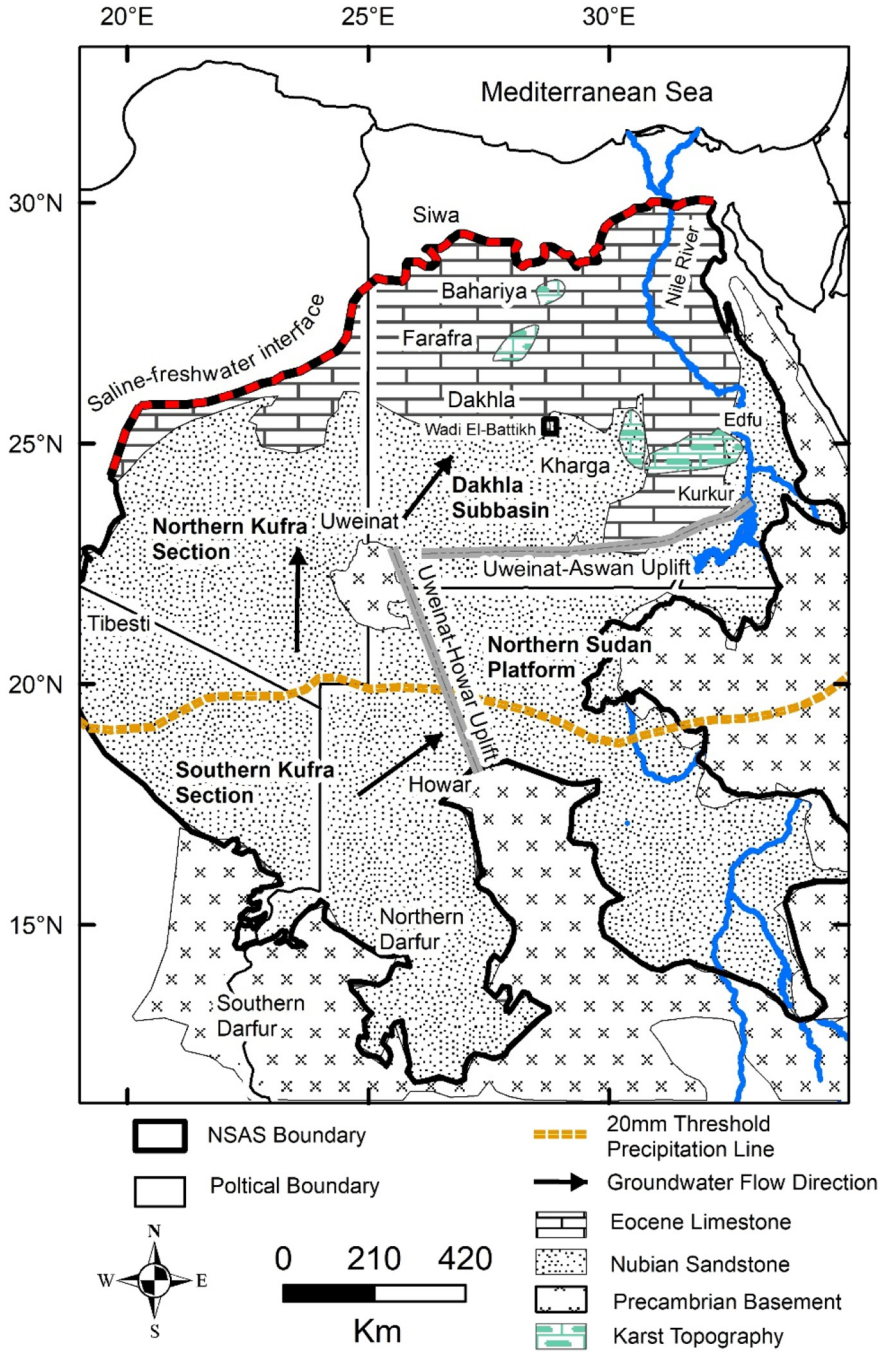

Fig. 1. (a) Location map showing the distribution of the NSAS and its subbasins (Dakhla, Kufra, and Northern Sudan Platform), the basement uplifts (Uweinat-Aswan, Uweinat-Howar), the 20 mm AAP threshold line, and the groundwater flow direction (Ball, 1927; Sanford, 1935).

3. Data processing

The three GRACE solutions which were applied (from April 2002 through June 2016) in this study are reported relative to a 2004–2009 mean baseline. The GRACE CSR-M solutions were derived using Tikhonov regularization (Save et al., 2016) and were resolved on a geodesic grid (grid size: 1 equatorial degree) (Save et al., 2012, 2016). No post-processing and/or filtering or application of empirical scaling factors was applied to the CSR-M or the JPL-M mascon solutions (Watkins et al., 2015; Save et al., 2016). Given the higher signal to noise ratio of the mascon solutions relative to the spherical harmonics (Watkins et al., 2015; Save et al., 2016; Scanlon et al., 2016), the CSR-M solutions were selected as the primary dataset for extracting trends over the investigated subbasins (Rodell et al., 2018). The secular trend in GRACE-derived TWS ($GRACE_{TWS}$) data was extracted by simultaneously fitting a trend and a seasonal term to each TWS time series. The variations (standard deviation) in trend values extracted from all three solutions (CSR-M, JPL-M, and CSR-SH) were considered to represent the uncertainty in the reported trend values (Scanlon et al., 2018; Rodell et al., 2018).

The spherical harmonics data was processed by replacing GRACE-derived C20 and degree-1 coefficients (Cheng et al., 2011; Swenson et al., 2008) and applying the glacial isostatic adjustment (GIA) correction using the GIA model (A et al., 2013). The noise was reduced at the basin scale by applying a destriping filter (Swenson and Wahr, 2006) and a Gaussian (250 km radius) smoothing filter (Wahr et al., 1998;

Swenson and Wahr, 2006). The scaling factor was applied to minimize the attenuation in TWS signal due to the post-processing of GRACE data (Landerer and Swenson, 2012; Long et al., 2015).

The contribution of the surface water to the Dakhla subbasin $GRACE_{TWS}$ was omitted by subtracting the $GRACE_{TWS}$ of a 120 km buffer zone surrounding Lake Nasser and the Tushka lakes (Fig. 2). This approach not only removes the contribution of the surface water, but also the contribution of the infiltration from the surface water in the immediate surroundings of Lake Nasser and the Tushka lakes. A calibrated two-dimensional groundwater flow model which was constructed to investigate the long-term hydrologic impacts of Lake Nasser in southwest Egypt revealed substantial infiltration in the immediate vicinity (<30 km) of the Lake amounting to 60 km^3 between years 1970 and 1984 and 40 km^3 between 1987 and 2000 (Sultan et al., 2013).

The periods used for the extraction of $GRACE_{TWS}$ trends were as follows: entire period (April 2002 through June 2016), dry (2002 through 2012), and wet (2013 through 2016) periods. The break points between the wet and dry periods were identified for each of the investigated subbasins using the Regime Shift Detection (RSD) method (Andersen et al., 2009; Reeves et al., 2007; Rodionov, 2004; Villarini et al., 2009). The phase image was generated by simultaneously fitting an annual cycle (sine and cosine) and trend terms for each $GRACE_{TWS}$ time series. The phase for each pixel is then calculated as the time (January to December) during which the maximum value was reached in the extracted annual cycle.

The spatial distributions of $GRACE_{TWS}$ trends were compared to other relevant geologic, topographic, and hydrologic data in a geographic information system (GIS) platform to identify sources of recharge and preferred pathways for groundwater flow and to investigate the aquifers' response to climate variability. The following data sets were generated over investigated areas (e.g., subbasins) and periods: (1) $GRACE_{TWS}$ trend images and time series extracted from $GRACE_{TWS}$ (Figs. 2, 3) to identify the spatial and temporal variations in $GRACE_{TWS}$; (2) Lake Nasser surface water levels (2002–2016) from the US Department of Agriculture Foreign Agricultural Service (USDA-FAS) global reservoir and lake monitoring database (GRLM; available at https://www.pecad.fas.usda.gov/cropexplorer/globalreservoir/), soil moisture data (2010 to 2016) from Soil Moisture and Ocean Salinity (SMOS) mission data (Kerr et al., 2001), and temporal head data (2005 to 2008) to investigate the response of groundwater levels and soil moisture content to fluctuations in Lake Nasser surface water (Figs. 4 and 5); (3) AAP rates and trends extracted from Tropical Rainfall Measuring Mission (TRMM) data (Huffman et al., 2007) and correlated with GRACE-derived products to investigate the factor(s) controlling the observed $GRACE_{TWS}$ variations; (4) $GRACE_{TWS}$ phase (Fig. 6) and difference images (Fig. 7) to investigate the direction and extent of TWS variations that are indicative of mass movement in dry and wet periods;

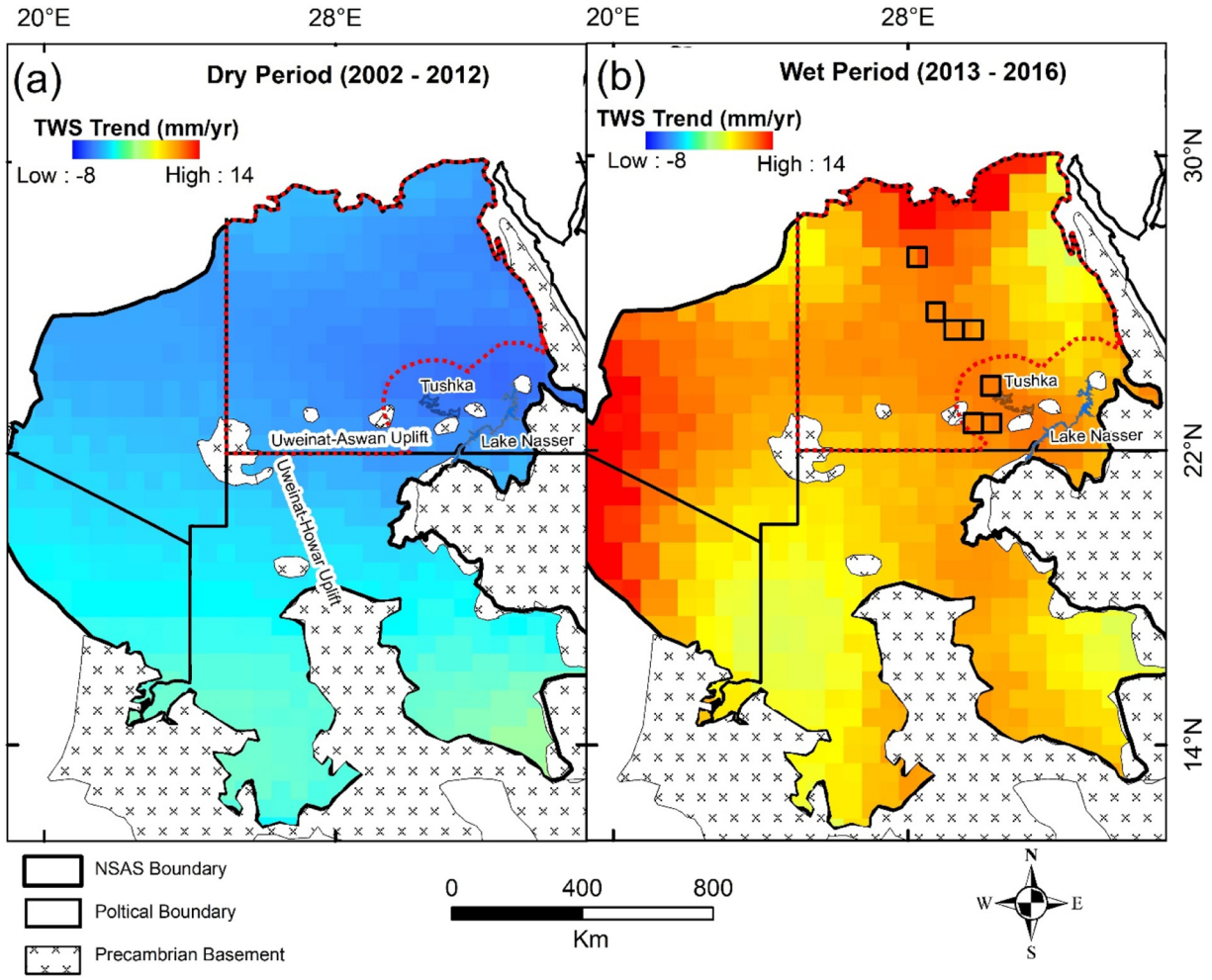

Fig. 2. Secular $GRACE_{TWS}$ trend image (mm/yr) over the NSAS. (a) Dry period (2002–2012). (b) Wet period (2013–2016). The red dashed line shows the distribution of the Dakhla subbasin less a polygon defined by a 120 km wide buffer zone surrounding Lake Nasser and the Tushka lakes. Also shown are the locations of 7 areas (outlined by black boxes) displaying temporal variations in soil moisture content similar to those observed over Wadi El-Batikh (Fig. 5a).

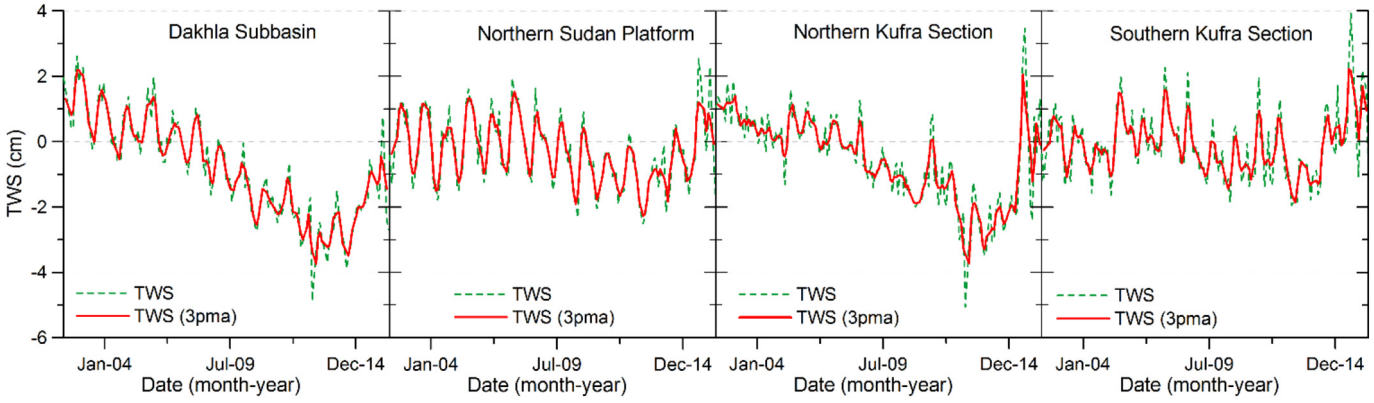

Fig. 3. $GRACE_{TWS}$ time series over Dakhla subbasin, Northern Sudan Platform, and Northern and Southern Kufra sections.

(5) geologic maps to extract fault traces; (6) Gravity Field and Steady-State Ocean Circulation Explorer (GOCE)-based global geopotential models (GGMs) to select the model having the least deviation from the terrestrial gravity data; (7) tilt derivative (TDR) product of the selected GGM (Fig. 8(a)) to extract the subsurface extensions of the fault traces and to map faults in sand-covered areas, and (8) isotopic composition for groundwater samples (Figs. 8b, 9) along the identified structures to test whether the identified structures represent preferred pathways for groundwater flow from Lake Nasser and from the Northern Sudan Platform to the Dakhla subbasin.

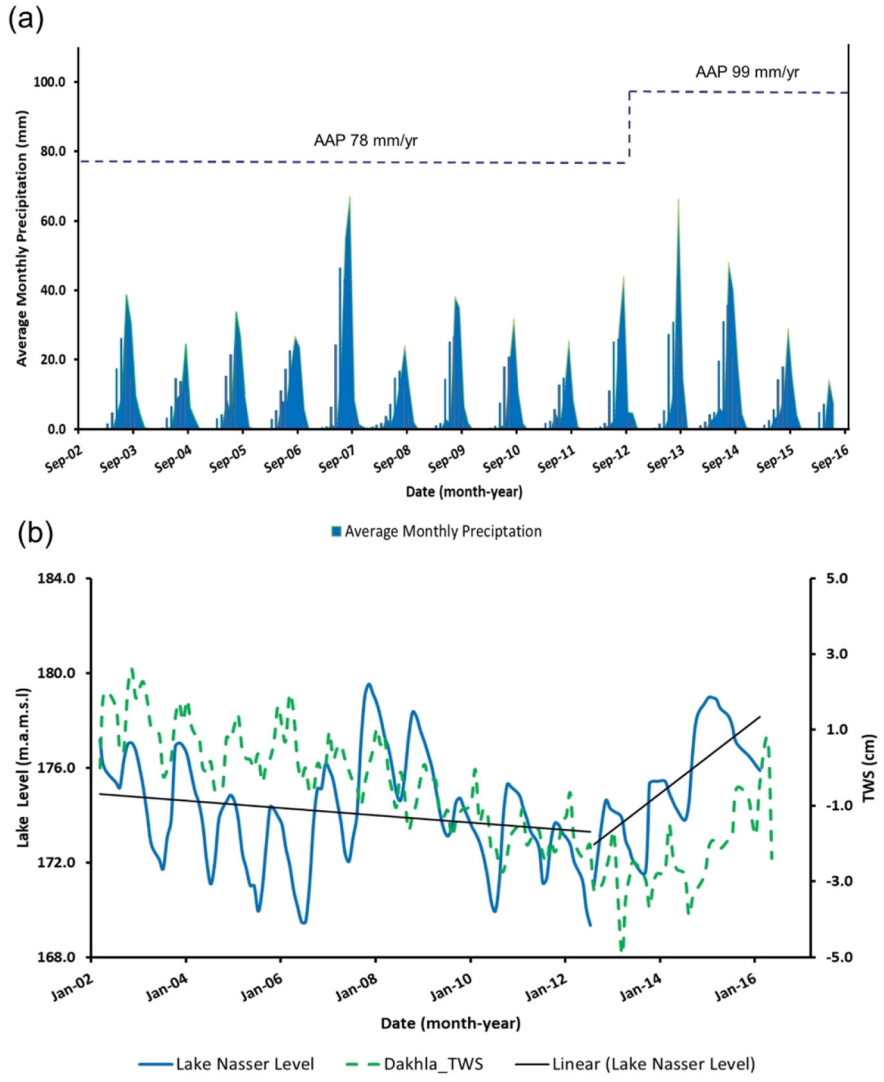

Fig. 4. (a) Average monthly and annual precipitation over the Northern Sudan Platform extracted from TRMM data for the dry and wet periods. (b) Time series for Lake Nasser surface water level (2002–2016) extracted from the GRLM database. For comparison, the $GRACE_{TWS}$ time series over the Dakhla subbasin is provided.

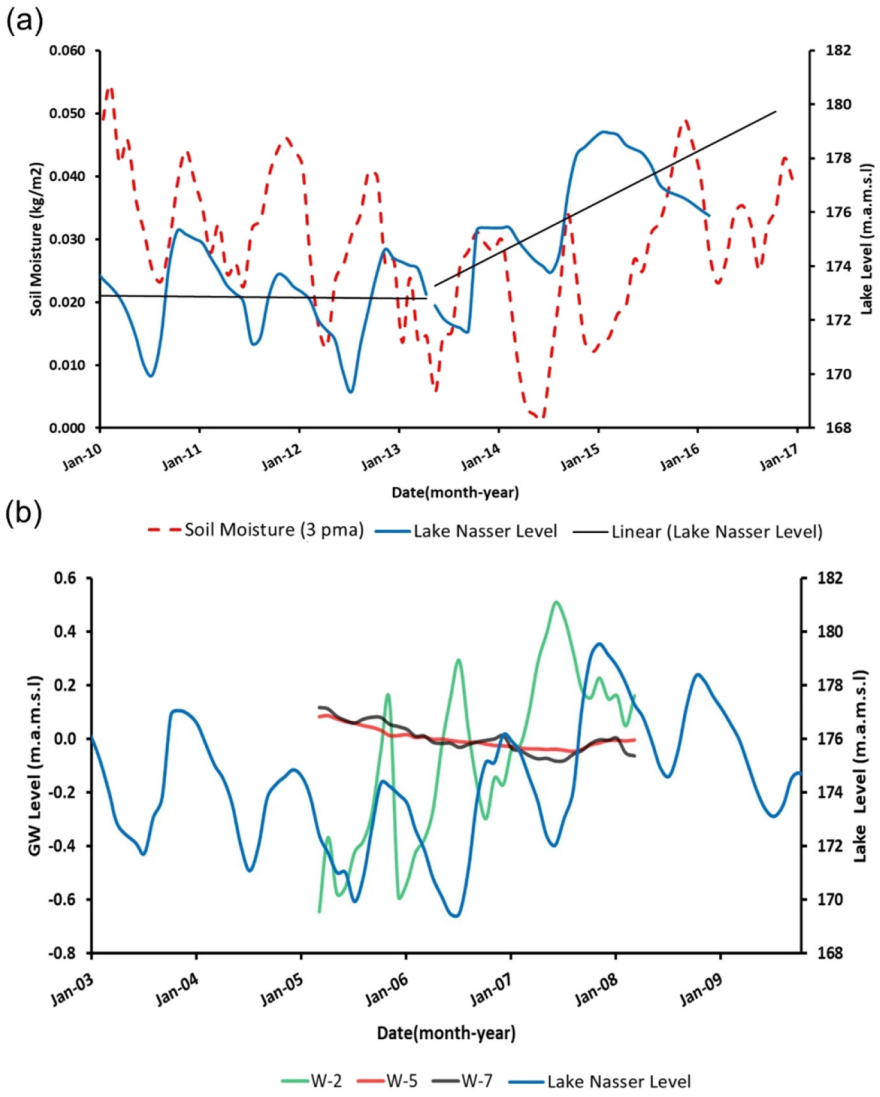

Fig. 5. Rapid response in groundwater level and soil moisture to fluctuations in Lake Nasser surface water levels. (a) Comparison of monthly (April 2005 to April 2008) soil moisture content from SMOS data acquired over Wadi El-Batikh with Lake Nasser surface water levels. (b) Comparison of monitoring well data (Wells # W-2, W-5 and W-7; 2005 to 2008) in East Uweinat area and surroundings to Lake Nasser surface water levels.

The TDR is a normalized phase derivative with first-order derivatives (Miller and Singh, 1994; Verduzco et al., 2004; Fairhead et al., 2011) and is defined as:

$$\text{Tilt derivative} = \tan^{-1}[\text{VDR}/\text{THDR}] \quad (1)$$

where, the VDR is the vertical derivative, and THDR is the total horizontal derivative. Due to the nature of the arctan trigonometric function, all amplitudes are restricted to values between $+\pi/2$ and $-\pi/2$ regardless of the amplitudes of the VDR and THDR (Verduzco et al., 2004; Fairhead et al., 2011). The TDR is independent of density since the VDR and THDR are functions of the density of the subsurface. The derivative is a powerful tool to identify subsurface structural edges (not density or magnetization), where the zero tilt indicates the location of rapid lateral changes in the density of basement materials (Oruc, 2010).

We collected 21 groundwater samples from wells tapping the NSAS in southern Dakhla subbasin for isotopic analyses (H and O; Table 1; Figs. 8b, 9). The DWT in the sampled wells ranged from 50 to 110 m. The wells were pumped for a minimum of 20 to 30 min before sampling of groundwater that were collected in 100 ml, tightly capped, polyethylene bottles. Stable isotope ratios of H and O in water were measured at the Stable Isotope Geochemistry Lab, Western Michigan University, USA, using Los Gatos Research (LGR) Off–Axis Integrated Cavity Output spectroscopy (off–Axis ICOS) technology. The isotopic data for samples are reported (Table 1) using the conventional delta (δ) notation, in units of permil (‰) deviation relative to Vienna standard mean ocean water (V-SMOW; Coplen, 1996), whereby

$$\delta_{\text{sample}}\,‰ = \left[R_{\text{sample}}/R_{\text{standard}} - 1\right] * 10^3 \quad (2)$$

and

$$R = {}^2\text{H}/{}^1\text{H or } {}^{18}\text{O}/{}^{16}\text{O} \quad (3)$$

For comparison purposes, we included additional reported analyses for groundwater samples from the Western Desert (Patterson et al., 2005; Thorweihe, 1986), and the Northern Sudan Platform (Thorweihe, 1986), surface water samples from Lake Nasser (Aly et al., 1993), and precipitation over the Northern Sudan Platform (Joseph et al., 1992).

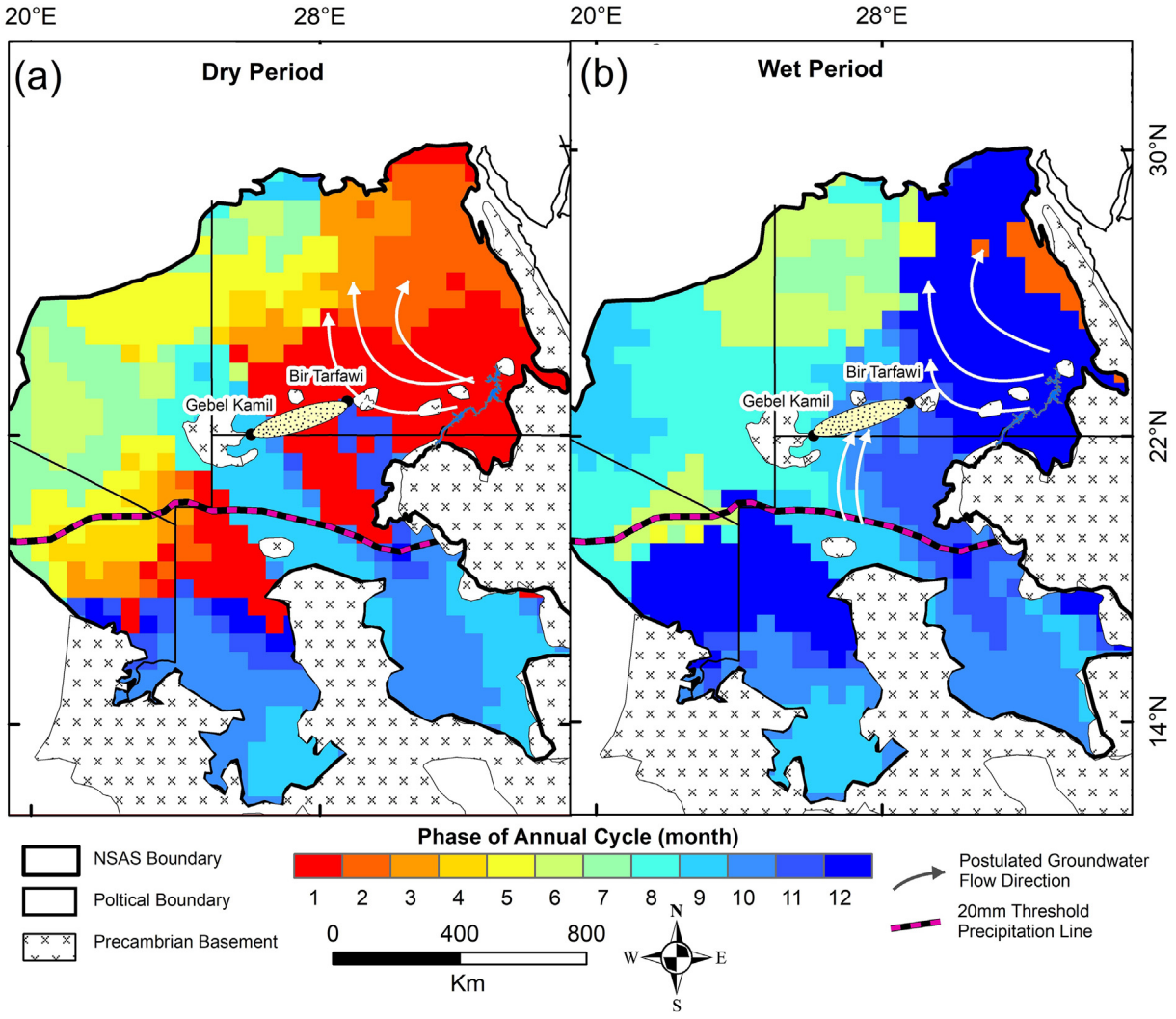

Fig. 6. The phase of the annual cycle derived from $GRACE_{TWS}$. (a) Phase during the dry period (2003−2012). (b) Phase during the wet period (2013–2015). The months of the year are represented by numbers (January: 1; December: 12).

4. Results and discussion

Fig. 2 shows the spatial distribution of the secular trends in $GRACE_{TWS}$ data over the NSAS and its subbasins throughout two climatic periods: a dry period extending from 2002 to 2012, followed by a wet period from 2013 to 2016. Fig. 3 shows the $GRACE_{TWS}$ time series over the Dakhla, the Northern Sudan Platform subbasins, and the Kufra sections. Positive trends indicate an increase in $GRACE_{TWS}$ with time, and negative trends indicate the opposite (Fig. 3 and Table 2). The Dakhla subbasin shows a depletion in $GRACE_{TWS}$ (-3.8 ± 1.3 mm/yr) during the period 2002 to 2012, followed by an increase in $GRACE_{TWS}$ of 7.8 ± 1 mm/yr during the period 2013 to 2016. The Northern Sudan Platform shows a near-steady state (-1.0 ± 1.2 mm/yr) during the earlier period followed by an increase during the later period (7.4 ± 0.3 mm/yr). The Southern Kufra section shows patterns similar to those of the Northern Sudan Platform, a near-steady state (-0.5 ± 1 mm/yr) during the earlier period followed by an increase in the later period (9.1 ± 2.2 mm/yr). The Northern Kufra section shows a pattern similar to the Dakhla subbasin, a depletion (-2.5 ± 2.2 mm/yr) followed by an increase in $GRACE_{TWS}$ (10.4 ± 1 mm/yr).

The observed increase in $GRACE_{TWS}$ in the Northern Sudan Platform and in the Southern Kufra during the wet period could be explained by an increase in precipitation during this period. The AAP over the Northern Sudan Platform during the wet period was high (99 mm/yr) compared to that during the earlier dry period (78 mm/yr), an increase of 27% (Table 2; Fig. 4(a)). A similar increase in precipitation was observed over the Southern Kufra during the wet period (Table 2; AAP for wet period: 115 mm/yr; dry period: 92 mm/yr). To the contrary, the AAP over the Dakhla subbasin was negligible during the dry (7.5 mm/yr) and wet periods (9.5 mm/yr), as was the precipitation over Northern Kufra section (Table 2; AAP for wet period: 6.7 mm/yr; dry period: 6.5 mm/yr). The increase in $GRACE_{TWS}$ over the Dakhla subbasin in the wet period amounted to 7.8 ± 1 mm/yr (total of 31.2 mm throughout wet period) and over the Northern Kufra section it was 10.4 ± 1 mm/yr (total of 41.6 mm throughout wet period). Going from the dry to the wet period, the AAP increased by 2 mm/yr (total of 8 mm throughout wet period) over the Dakhla subbasin and by 0.2 mm/yr (total of 0.8 mm throughout wet period) over the Northern Kufra. Previous work has shown that recharge in the Egyptian deserts ranges from 11 to 31% of the total precipitation (Milewski et al., 2009). Even if we were to assume that all the added precipitation during the wet period ended up as recharge, we still cannot account for the observed increase in $GRACE_{TWS}$ over the Dakhla subbasin and the Northern Kufra section. Thus, the observed increase in $GRACE_{TWS}$ over these two areas during the wet period cannot be attributed to an increase in precipitation, nor could it be due to an increase in soil moisture, given that precipitation remained negligible throughout the investigated

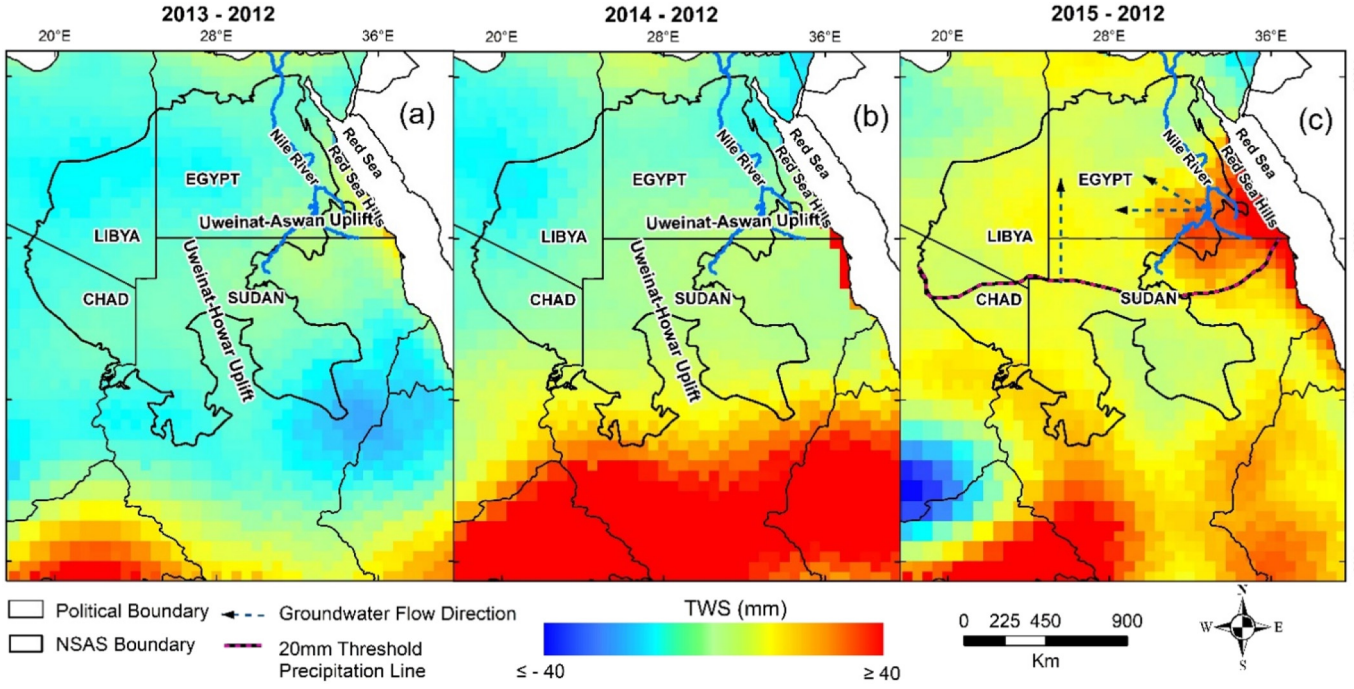

Fig. 7. Difference images showing a progressive increase in TWS and mass movement during the wet period from the south to the north and from Lake Nasser to its surroundings. (a) Difference image between the AA $GRACE_{TWS}$ for 2013 and that for 2012. (b) Difference image between the AA $GRACE_{TWS}$ for 2014 and that for 2012. (c) Difference image between AA $GRACE_{TWS}$ 2015 and that for 2012. Also shown is the 20 mm AAP threshold line and groundwater flow distances measured from the source areas (Lake Nasser and areas receiving AAP >20 mm in Northern Sudan Platform), represented by the length of arrows.

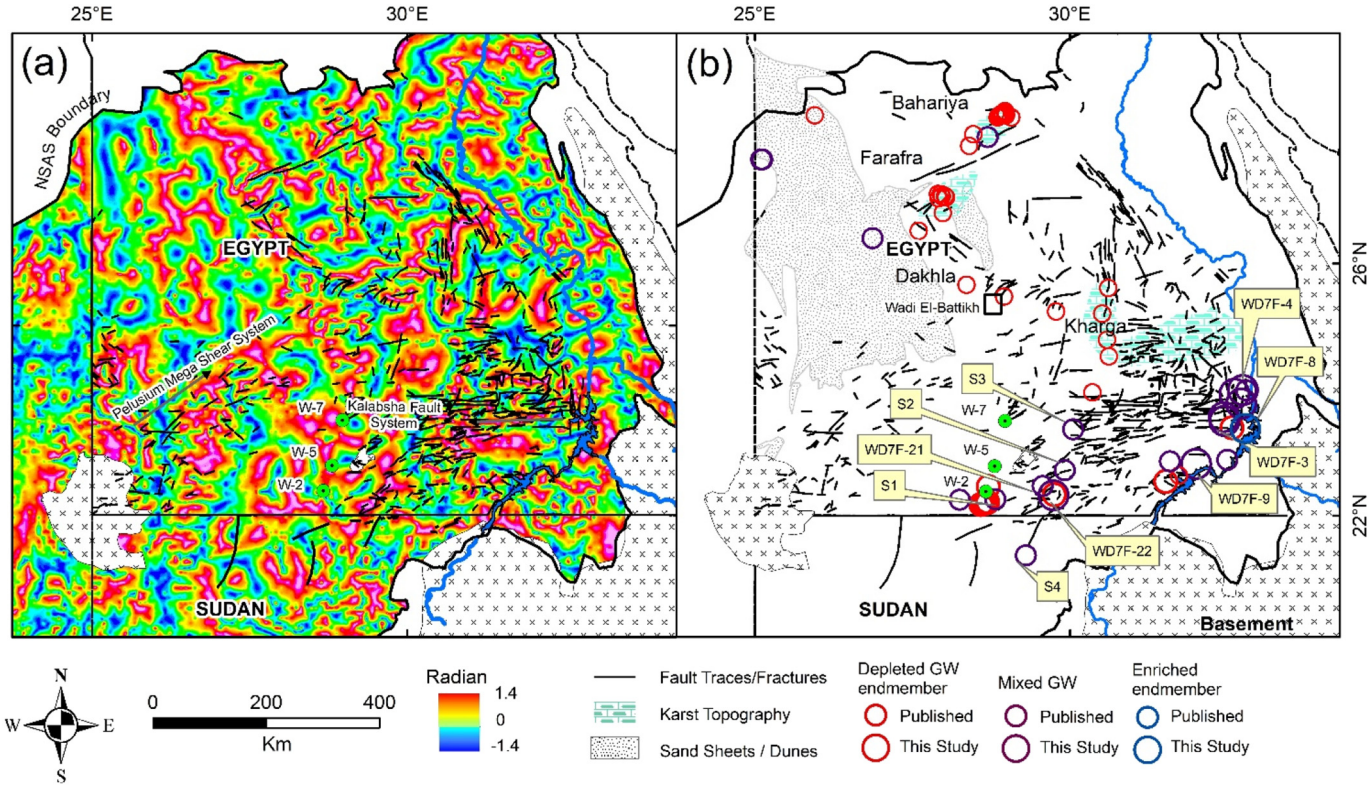

Fig. 8. (a) TDR image showing the distribution of inferred deep-seated northwest, northeast, north-south, and east-west trending lithologic contacts and/or faults mapped along zero-tilt lineaments (yellow colors). (b) Interpretation map showing the distribution of fault traces and fractures (El-Hinnawi et al., 2005, 2006; GRAS, 1988). Note the correspondence of the zero-tilt lineaments with the fault traces. The complex of intersecting structures can represent preferred pathways for groundwater flow. Also shown are the spatial distribution of color-coded isotopic compositions for our groundwater samples (large open circles) from productive wells tapping the NSAS and reported isotopic compositions for the NSAS paleowaters from the Western Desert (small open circles).

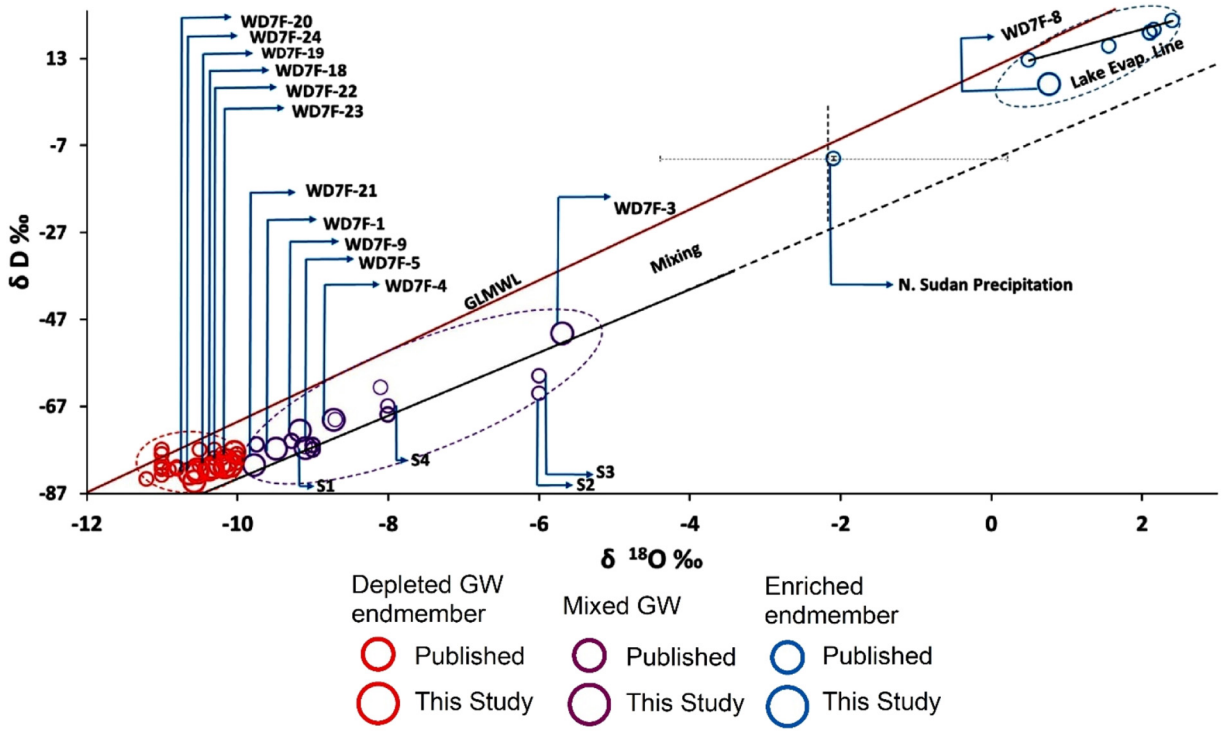

Fig. 9. The isotopic composition of our samples (large open circles) plotted on a δD versus $\delta^{18}O$ plot and compared to groundwater (small open red and purple circles; Patterson et al., 2005; Thorweihe, 1986) and modern precipitation (open blue circle; mean ± 1 SD) from northern Sudan (Khartoum IAEA station; Joseph et al., 1992). Also shown are the paleo meteoric water line (MWL), $\delta D = 8\ \delta^{18}O + 6.3$ (Dietzel et al., 2014) and global meteoric water line (GMWL), $\delta D = 8\ \delta^{18}O + 10$ (Craig, 1961) and evaporation line for Lake Nasser (Aly et al., 1993).

period. The observed increase in $GRACE_{TWS}$ will have to be related to an increase in surface and/or groundwater storage.

There are no major rivers in the Northern Kufra section, and thus the observed increase in $GRACE_{TWS}$ in the Northern Kufra section during the wet period would have to be due to groundwater flow from the Southern Kufra section. There is one major river that flows in the Dakhla subbasin, the Nile River (Fig. 1). During the wet periods one would expect increased runoff from the source areas in the Ethiopian highlands, impoundment of excess Nile River water in Lake Nasser, elevated lake levels, and an increase in the surface water storage. Investigating the time series of Lake Nasser level fluctuations for the period between 2002 and 2016 (Fig. 4(b)) indicated that indeed this is the case. We observe a progressive rise in average annual lake levels from 172 m.a.m.s.l. in 2012 to 178 m.a.m.s.l in 2015 (Fig. 4(b)) as well as an increase in its area. Examination of the temporal Landsat thematic mapper (TM) data over Lake Nasser revealed, that its area increased from 3622 km^2 in 2012 to 4530 km^2 in 2016. Likewise, $GRACE_{TWS}$ trends for a 120 km wide polygon centered over Lake Nasser increased from −4.1 ± 0.3 mm/yr (−0.2 ± 0.01 km^3/yr) during the dry period to 8.6 ± 1.5 mm/yr (0.5 ± 0.08 km^3/yr) in the wet period. One would also expect

Table 1
Locations and O and H isotopic compositions for groundwater samples from wells tapping the NSAS in the southern parts of the Western Desert and in areas proximal to Lake Nasser.

Sample ID	Name	Area	Longitude E	Latitude N	δ D (‰)	$\delta^{18}O$ (‰)
WD7F-3	Seal PNK	Lake Nasser	32.44000	23.5600	−50.2	−5.69
WD7F-4	Kurkr	Lake Nasser	32.74091	23.98783	−70.1	−8.72
WD7F-5	Khor Galal	Lake Nasser	32.71683	23.77234	−76.6	−9.09
WD7F-6	GW1	Lake Nasser	32.57000	23.39000	−79.4	−10.14
WD7F-7	PSK	Lake Nasser	32.45000	23.50000	−77.4	−10.04
WD7F-9	Garef Hussien	Lake Nasser	31.99975	22.81808	−72.6	−9.17
WD7F-23	Research Desert 2	Lake Nasser	31.51756	22.53808	−81.0	−10.17
WD7F-24	Magnetic Station	Lake Nasser	31.54392	22.49089	−84.2	−10.58
WD7F-8	DW3	Lake Nasser	32.84366	23.34897	7.1	0.77
WD7F-11	East Oweinat 3	East Uweinat	28.68989	22.20419	−79.5	−10.21
WD7F-12	East Oweinat 5	East Uweinat	28.64700	22.19136	−79.7	−10.15
WD7F-13	East Oweinat 7	East Uweinat	28.65386	22.19406	−82.2	−10.53
WD7F-14	East Oweinat 9	East Uweinat	28.64017	22.18939	−81.5	−10.54
WD7F-15	East Oweinat 11	East Uweinat	28.62564	22.18514	−81.1	−10.33
WD7F-16	East Oweinat 12	East Uweinat	28.59178	22.17639	−81.5	−10.38
WD7F-17	East Oweinat 13	East Uweinat	28.58586	22.17297	−80.6	−10.09
WD7F-18	East Oweinat 16	East Uweinat	28.67961	22.21419	−80.4	−10.24
WD7F-19	East Oweinat 14	East Uweinat	28.68903	22.21703	−81.0	−10.34
WD7F-20	Army	East Uweinat	28.70262	22.45915	−82.4	−10.64
WD7F-21	Darb Al Arbaein 1	Darb Al Arbaein	29.73906	22.31775	−75.1	−9.28
WD7F-22	Darb Al Arbaein 2	Darb Al Arbaein	29.74925	22.32800	−80.7	−10.16

Table 2
Precipitation and terrestrial water storage over the NSAS throughout the dry (2002–2012) and wet (2013–2016) periods.

Area	Area	Dry period (2002–2012)				Wet period (2013–2016)			
		[a]ΔTWS		[b]AAP		[a]ΔTWS		[b]AAP	
	km^2	mm/yr	km^3/yr	mm/yr	km^3/yr	mm/yr	km^3/yr	mm/yr	km^3/yr
Dakhla sub-basin	67×10^4	-3.8 ± 1.3	-2.5 ± 0.9	7.5	5	7.8 ± 1	5.2 ± 0.7	9.5	6.4
Southern Kufra section	64×10^4	-0.5 ± 1	-0.3 ± 0.06	92	59.5	9.1 ± 2.2	5.9 ± 1.4	115	74.3
Northern Kufra section	25×10^4	-2.5 ± 2.2	-0.6 ± 0.6	6.5	1.7	10.4 ± 1	2.7 ± 0.3	6.7	1.7
Northern Sudan platform	43×10^4	-1 ± 1.2	-0.5 ± 0.6	78	34.2	7.4 ± 0.3	3.3 ± 0.1	99	43.5

[a] ΔTWS: Change in terrestrial water storage.
[b] AAP: Average Annual Precipitation.

increased infiltration and recharge, a rise in groundwater levels, and enhanced down gradient groundwater flow during wet periods. Using a calibrated two-dimensional groundwater flow model, Sultan et al. (2013) investigated the long-term hydrologic impacts of Lake Nasser in southwest Egypt. Their model outputs showed that during a similar rise in Lake Nasser surface water levels (water levels: 170 m above mean sea level [m.a.m.s.l] in 1992; 179 m.a.m.s.l in 1995) recharge increased from 0.7 km^3/yr to 6 km^3/yr. We attribute the increase in $GRACE_{TWS}$ in the Dakhla subbasin during the wet period to increased infiltration and groundwater flow from Lake Nasser and from the Northern Sudan as well.

We test the above-mentioned hypothesis (the nature of the source areas) and the direction and extent of mass movement during dry and wet periods using phase and difference images extracted from temporal $GRACE_{TWS}$ data. The phase diagrams display the month in which the maximum $GRACE_{TWS}$ value was attained for each pixel, in the dry period (Fig. 6(a)), and in the wet period (Fig. 6(b)). Fig. 6(a) shows that Lake Nasser and its surroundings, extending some 600 km to the west and 300 km to the north, attained their maximum $GRACE_{TWS}$ values in the month of January. To the north and northwest of these areas, phase values transition from the month of January to February, then March followed by April, and ending by the month of July in the extreme northwest of the Dakhla subbasin. The observed phase over Lake Nasser and its immediate surroundings are to be expected given that the lake surface water levels peak in the months of December and January (Figs. 4 and 5). One interpretation that is consistent with the observed phase patterns during the dry period is that Lake Nasser is the main source of recharge, with modest to minimal recharge from the south, and that mass movement is extensive and rapid (hundreds of km/yr along preferred directions). During the wet period, a maximum phase is observed over Lake Nasser in the same approximate period (December instead of January), yet the progressive transition in phase from Lake Nasser outwards throughout major sections of the Dakhla subbasin that was observed during the dry period is absent. Instead, we observe a maximum phase over source areas in northern Sudan (south of the 20 mm threshold precipitation line) during the reported peak precipitation periods (August and September; Fig. 4(a)). To the north and northeast of this area the phase transitions progressively from the months of September/August to October, followed by November, and ends up in December to the east and northeast of the Dakhla subbasin, where apparently recharge from Lake Nasser is underway at the same approximate time period (December) in the year. One plausible interpretation of these patterns is that during wet periods, the Dakhla subbasin receives rapid and extensive groundwater flow from the Northern Sudan Platform and from Lake Nasser. The inferred rapid overall groundwater flow directions in both the wet and dry periods are represented by arrows on Fig. 6. The lines satisfy a number of conditions: they originate from the proposed sources areas, a progressive increase in phase and decrease in amplitude is observed along their length, and they terminate where the advocated phase transitions are disrupted.

If the advanced conceptual model is true, one would expect to observe a progressive increase in the $GRACE_{TWS}$ downgradient from the source areas, namely from the Southern Kufra section towards the Northern Kufra section and from the Northern Sudan Platform and from Lake Nasser towards the Dakhla subbasin throughout the wet period. One way to examine these postulated spatial variations in $GRACE_{TWS}$ throughout the wet period is through the construction of difference images between the average annual $GRACE_{TWS}$ (AA $GRACE_{TWS}$) for: (1) 2013 and 2012 (Fig. 7(a)), (2) 2014 and 2012 (Fig. 7(b)), and (3) 2015 and 2012 (Fig. 7(c)). Inspection of Fig. 7 shows a progressive increase in $GRACE_{TWS}$ and mass movement from the source areas, namely Lake Nasser, and from northern Sudan towards the Dakhla subbasin. Comparison of Fig. 7(a–c) shows that by 2015, almost all the Dakhla subbasin shows an overall increase in $GRACE_{TWS}$, with the largest increase (>20 mm) observed over areas extending up to 400 km from the source areas (Lake Nasser and areas south of the 20 mm AAP threshold line; Fig. 7(c)). These distances are represented by the length of the dashed arrows in Fig. 7(c). It is here assumed that recharge of the NSAS will occur in areas to the south of the line but not to the north of it, where the limited precipitation is less likely to recharge the NSAS and more likely to be lost to evaporation. It is worth mentioning that the groundwater flow from the Northern Sudan Platform subbasin to the Dakhla subbasin is limited during the dry periods, given the presence of an east-west–trending basement uplift, the Uweinat-Aswa (Mohamed et al., 2017). Apparently, though, the flow becomes less restricted during the wet periods along windows found in areas within the uplift, where the basement is deep, the aquifer is thick. One of these windows is found to the east of the Uweinat outcrop at the borders of Egypt, Sudan, and Libya (Fig. 1); the window is 225 km wide (Fig. 6), the basement at this location is up to 370 m deep, and the average depth to water table is 10–50 m (Mohamed et al., 2017).

Additional evidence for the advocated model comes from the rapid response in groundwater levels in wells distant from Lake Nasser that are located along, or proximal to, the preferred pathways for groundwater flow and by a similar rapid response in the soil moisture content within areas characterized by near-surface groundwater levels (<2 m). One of these areas is Wadi El-Battikh (refer to Figs. 1 and 8(b) for location). It is located some 450 km to the west of Lake Nasser and 600 km from the potential source areas in northern Sudan (Fig. 1); because of its shallow groundwater table, farmers grow watermelons in these areas. Fig. 5(a) shows a general correspondence between the soil moisture content in Wadi El-Battikh and Lake Nasser surface water levels. For example, Lake Nasser surface water levels started to rise from (170 m) in August 2012 and peaked at 179 m in April 2015; for the following three years (2012 to 2015), soil moisture fluctuations in Wadi El Battikh corresponded to those in Lake Nasser, but lagged by 6–8 months. The Wadi El-Batikh area is characterized by major faults (northwest-southeast trending faults; El-Hinnawi et al., 2005; Fig. 8(b)) where these faults intersect the escarpment, promontories, and embayments at theater head valleys, indicating groundwater discharge along the extension of these faults (Abotalib et al., 2016). Several locations within the Western Desert display temporal variations in soil moisture content similar to those observed over Wadi El-Batikh. Specifically, they show stable or decreasing soil moisture content during the dry period followed by an increase during the wet period. Seven of these locations are displayed in Fig. 2b. The identified locations are all in lowlands, in

areas where groundwater levels are shallow, and where sub-vertical, deep-seated faults were mapped; the faults act as conduits for ascending deep groundwater within the confined sections of the NSAS (Abotalib et al., 2016).

A similar correspondence and rapid response to fluctuations in Lake Nasser was observed in a monitoring well (well W-2) located some 280 km to the west of Lake Nasser (Figs. 1 and 8(b)). A rise in the lake's surface water level started in August 2005 and peaked at 179 m in January 2008; for the following three years (April 2005 to April 2008), fluctuations in groundwater levels in well W-2 corresponded to those in Lake Nasser, but lagged by 4–6 months (Fig. 5(b)). In contrast, two other proximal wells (W-5 and W-7, <150 km from well W-2) showed no response to fluctuations in Lake Nasser surface water levels (Fig. 5(b)). One interpretation for the reported differences in monitoring well response is that well W-2, but not wells W-5 and W-7, is probably located along the postulated extension of the east-west trending Kalabsha fault system, or along the extension of a northeast-trending strand of the Pelusiam fault system (Fig. 8(b)), both considered here to be potential preferred pathways for groundwater flow. One should expect a general (but not a one-to-one) correspondence between the lag time extracted from the phase analysis of $GRACE_{TWS}$ and that extracted from the groundwater levels and soil moisture data. The former provides the average lag time over large areas, whereas the latter reflects the local nature of the flow pathways that feed the examined locations. Unfortunately, very limited monitoring well data is available for the Western desert of Egypt temporally and spatially to further test our suggestions.

If the advocated seasonal and interannual mass movements in the wet and dry years are valid, one would have to invoke a rapid mass movement of hundreds of kilometers in the investigated periods. That is difficult to reconcile if the groundwater flow was through porous media under laminar Darcian flow, even if the media had exceptionally high effective porosity and permeability. One way to achieve this rapid mass movement is for groundwater flow to occur as rapid turbulent non-Darcian flow within high transmissivity zones within fractured systems (faults/shear zones) and karstic textures. Very high hydraulic conductivities (0.01 to 1 m/s; Bear, 1972) were reported for densely fractured bedrocks using integrated theoretical and experimental approaches. Tracer experiments in fractured aquifers indicated that groundwater flow could attain velocities several orders of magnitude higher than natural groundwater flow through porous media (Lapcevic et al., 1999), and the flow velocity in the individual fractures can be extremely high (>1 m/s; Kohl et al., 1997). Such high flow velocities in fractures are maximized within areas characterized by high hydraulic gradients such as those surrounding dam-generated artificial lakes (Qian et al., 2005), Lake Nasser being one of these areas (hydraulic gradient: 0.0014; Alfaran, 2013). Groundwater flow velocities exceeding 2 km/day were measured in fissured and karstic chalk aquifers in the Hampshire Basin, south Hampshire (Atkinson & Smith, 1974). Using a tracer test, Banks et al. (1995) measured similar high groundwater flow velocities (5.8–6.8 km/day) in a karstic system within a chalk aquifer in Stanford Dingley, Berkshire, in southern England. They attributed these high velocities to secondary fissure flow systems developed by preferential dissolution along discontinuities (e.g., bedding planes and fractures) producing high transmissivity zones (Banks et al., 1995). The advocated rapid flow for the NSAS contrasts with the much slower flow (0.05–0.5 cm/day) within the Nubian Sandstone matrix (Patterson et al., 2005; Sturchio et al., 2004; Sultan et al., 2013). It is the former type of groundwater flow, not the latter, that is causing the observed temporal and spatial variations in $GRACE_{TWS}$ during the wet period in the Dakhla subbasin and in the Northern Kufra section. For this to be true, one would expect to observe extensive networks of interconnected structures and/or karstic topography.

The Dakhla subbasin is dissected by sub-vertical, deep-seated basement faults, many of which were reactivated by later tectonic activities (Neev et al., 1982; Sultan et al., 2007a). These include: (1) north-south—trending accretionary structures, (2) northwest-southeast—trending Najd faults in the eastern sections of the Western Desert, (3) east-west—trending Kalabsha and Seiyal fault systems in the southern parts of the Western Desert, and (4) northeast-southwest—trending Pelusium faults in the western sections of the Western Desert (Hermina, 1990; Khan et al., 2014; Neev, 1975; Neev et al., 1982; Thurmond et al., 2004). We correlated the distribution of fault traces and fractures (El-Hinnawi et al., 2005, 2006; GRAS, 1988) with potential fault locations extracted from TDR maps of gravity data (Oruc, 2010; Verduzco et al., 2004). The TDR filter was applied to enhance the geophysical signal of the basement structures (Oruc, 2010). The TDR filter was applied to the gravity data derived from Eigen-6C4 GGM; the latter was found to have the least deviation (9.122 mGal) from the terrestrial gravity data (21,262 sites) for the study area. The applied approach (selection of model showing minimum deviation from terrestrial gravity data) was adopted after Elsaka et al. (2016).

Fig. 8(a) is a TDR map for the Dakhla subbasin and surroundings showing radian values between −1.4, 0, and +1.4. On this map the red color reflects positive tilt values, the blue shades indicate negative tilt values, and the yellow colors delineate areas with zero tilt. The zero-tilt lineaments could indicate the location of lithologic contacts and/or faults (Verduzco et al., 2004; Oruc, 2010). Also plotted on Fig. 8 are fault traces exceeding 10 km in length (El-Hinnawi et al., 2005, 2006). Fig. 8(a) shows numerous north-south, northwest-southeast, northeast-southwest, and east-west trending linear features, and many of the zero-tilt lineaments coincide with the mapped fault traces. Inspection of geologic maps (e.g., Conco, 1987; El-Hinnawi et al., 2005, 2006), and our analysis of satellite imagery (Landsat TM) revealed that large sections of the Western Desert are covered by sand dunes and sheets, and thus fault traces were only mapped in the dune and sand sheet-free areas (Fig. 8(b)). Approximately two-thirds of the Dakhla subbasin is covered by marine limestone plateau which extends west of the Nile Valley (Fig. 1; Conco, 1987). The limestone outcrops are largely formed of Cretaceous chalk and Eocene limestone, many of which were described as having karstic features (e.g., dissolution caves, speleothems, chalk pillars, and flowstones). They were reported along fractures and joints west of Lake Nasser (e.g., El Gammal, 2010; Halliday, 2003; Ruggieri, 2001; Waltham, 2001), along, and proximal to, the road from the Farafra Oasis to the Bahariya Oasis, in the Kharga and Siwa depressions, and from the Kurkur area (Figs. 1 and 3(b); Aref et al., 1987; Butzer, 1965; El Gammal, 2010; Mostafa, 2013; Ruggieri, 2001; Waltham, 2001). The high inferred groundwater flow velocities for the NSAS is common in fractured and karstic aquifers. These reported faults and karst systems in the Dakhla subbasin represent preferred pathways (Mohamed et al., 2017) as well as vertical passages for groundwater connection between the NAS and the overlying PNAS (Abotalib et al., 2019; Mohamed et al., 2017). Given the densely mapped fault and karst networks, and building on the observations extracted from GRACE, altimetry, SMOS, and monitoring well data, we advocate similar systems in our study area, where extensive networks of deep-seated fault systems and karstic topography provide preferred and rapid pathways (or hydraulic conduits) for groundwater flow across large sections of the Dakhla subbasin.

If our conceptual model is true one could expect the isotopic composition of groundwater within, or proximal to, the preferred pathways to reflect mixing between depleted NSAS groundwater and modern waters from Lake Nasser and from precipitation over recharge areas in the Northern Sudan Platform. The isotopic composition of the collected samples were compared to those of Lake Nasser surface water (Aly et al., 1993), modern precipitation (mean ± 1 Standard Deviation [1S]: δD: $-10.0 \pm 15.7‰$; $\delta^{18}O$: $-2.09 \pm 2.3‰$) over recharge areas in the Northern Sudan Platform (Joseph et al., 1992), and reported groundwater composition (Patterson et al., 2005; Thorweihe, 1986) across the Western Desert (Figs. 8(b), 9). The majority of our groundwater samples (e.g., WD7F-20, WD7F-19, WD7F-18, WD7F7-24, and WD7F-23; Table 1, Fig. 9) had depleted isotopic compositions (δD: −84.2 to

−80.4‰; $\delta^{18}O$: −10.6 to −10.1‰) that are typical of NSAS paleowater composition (Abotalib et al., 2016; Mohamed et al., 2017; Sultan et al., 2007b), whereas the composition of a number of our groundwater samples (e.g., WD7F-3, WD7F-4) from wells proximal (<30 km) to Lake Nasser are consistent with depleted NSAS groundwater mixing with enriched Lake Nasser water (Figs. 8(b), 9; Table 1). One of our groundwater samples (WD7F-8) that was collected only a few kilometers west of Lake Nasser yielded an isotopic composition (δD: 7.1‰; $\delta^{18}O$: 0.77‰) that approaches that of Lake Nasser surface water (Figs. 8(b), 9).

A considerable number of groundwater samples, both ours and reported by others, from East Uweinat and Darb Al Arbaein (e.g., WD7F-21, S1, S2, and S3), approximately 200–300 km from Lake Nasser show evidence of mixing with a more enriched endmember (Figs. 8(b), 9). Although it is possible that the enriched samples in these two areas received contributions from Lake Nasser through infiltration and preferred groundwater flow along east-west trending faults and shear zones (Fig. 8), it is also possible that the source of their modern contributions is groundwater flow from the south that originated as modern precipitation over the Northern Sudan Platform (Fig. 3). This hypothesis is supported by the observed similarity in isotopic compositions of enriched samples from East Uweinat and Darb Al Arbaein to samples (e.g., S4) from northern Sudan (Figs. 8(b), 9), and by the fact that the enriched compositions from East Uweinat could be explained by mixing between depleted NSAS groundwater and precipitation over northern Sudan (Fig. 9). Some of these enriched samples around Lake Nasser and in East Uweinat were collected only hundreds of meters away from others that yielded typical NSAS depleted isotopic signatures (e.g. WDF-21, 22; Figs. 8(b), 9). One likely explanation is that the former samples, not the latter samples, were collected from wells lying on, or proximal to, one of the preferred groundwater flow pathways.

During the wet periods, groundwater recharge intensifies through infiltrated precipitation in the south and through infiltration from Lake Nasser and mixes with the extensive depleted fossil groundwater of the NSAS. The total water reserves in the Dakhla subbasin are estimated at 154,716 km^3 (Bakhbakhi, 2006), whereas the combined increase in $GRACE_{TWS}$ due to the groundwater flow from Lake Nasser and from the Northern Sudan Platform is here estimated at ~8.5 km^3/yr. Thus, one should not expect to observe evidence for mixing from samples collected across the entire Dakhla subbasin. Instead, evidence for mixing is likely to be detected in samples collected from wells that are located on, or proximal to, these preferential pathways. Examination of Fig. 3 supports this suggestion; a number of enriched samples (e.g., WD7F-9, WD7F-3, S3; Fig. 8(b)) lie on east-west trending faults originating at or near Lake Nasser, and others (e.g., S4, WD7F-21, S2, S3; Fig. 8(b)) lie on north-south trending faults originating in northern Sudan.

We offer a conceptual model (Fig. 10) that is consistent with the above-mentioned field and isotopic observations and our earlier

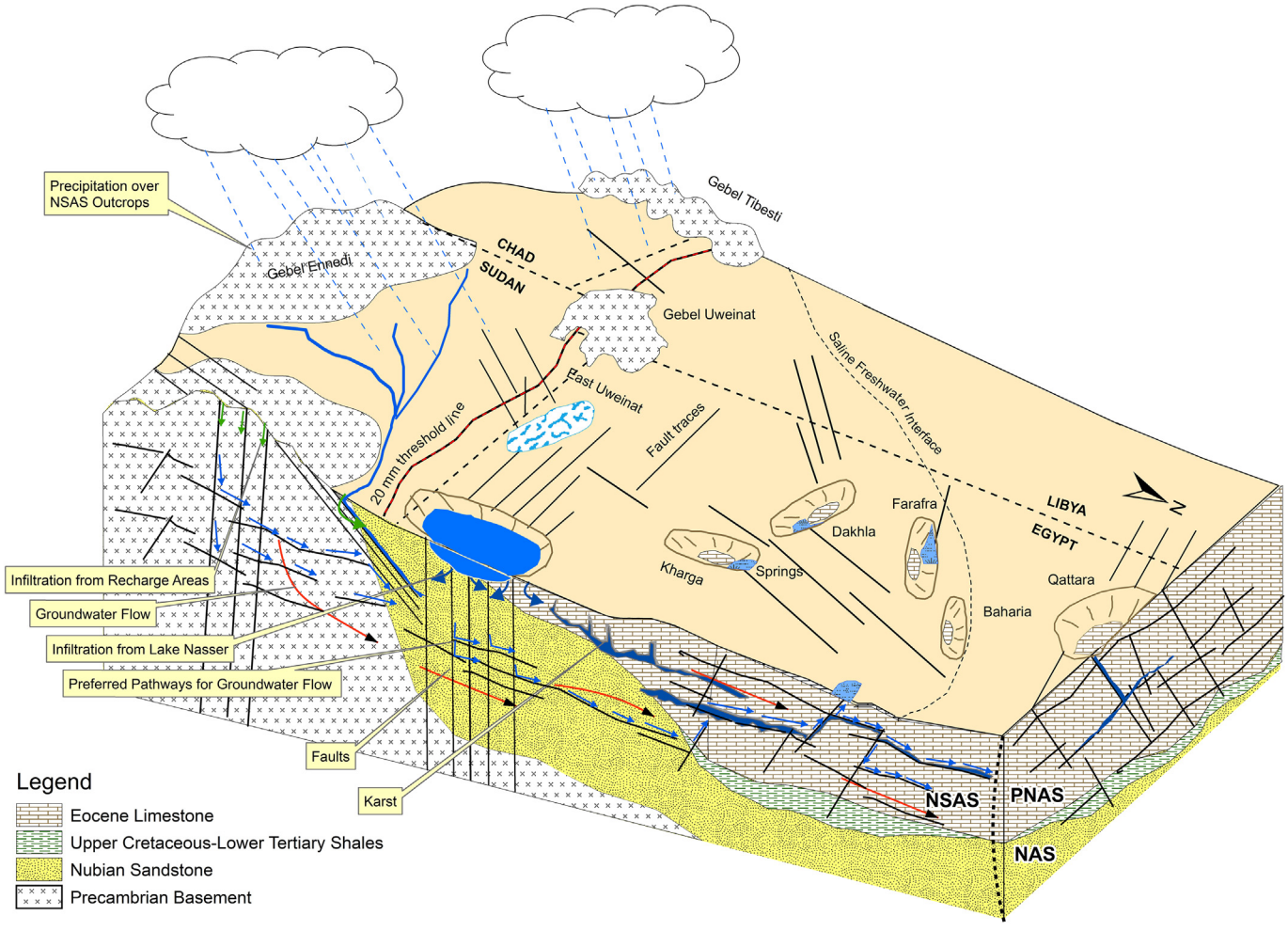

Fig. 10. Block diagram showing our hydrological conceptual model for the NSAS where faults and karst serve as preferred groundwater flow conduits allowing groundwater flow to discharge areas. The figure shows on the surface and in cross section the locations of infiltration and recharge from precipitation in the Northern Sudan Platform south of the 20 mm AAP threshold line (green arrow) and from Lake Nasser (blue arrow), areas of natural discharge (oases in Western Desert), preferred pathways for groundwater flow (interconnected faults and karst topography), and groundwater flow direction flow (red arrows).

GRACE-related temporal and spatial variations. We advocate that during the dry period, Lake Nasser is the main source of recharge for the Dakhla subbasin with modest to minimal recharge from the Northern Sudan Platform. The lake receives on an annual basis added river flow during the flood season (month of December/January) that increases Lake Nasser surface water level, infiltration, recharge, and groundwater flow from the lake to the Dakhla subbasin. During the wet periods, Lake Nasser receives higher surface water flow compared to those received during dry periods, leading to excessive rise in Lake Nasser surface water level, infiltration, recharge, and groundwater flow from the lake to the Dakhla subbasin. In contrast to the dry periods, the Dakhla subbasin receives in the wet period additional recharge from the south. Precipitation over the Northern Sudan Platform increases, as does infiltration, recharge, and groundwater flow from the south (Northern Sudan Platform) towards the Dakhla basin. During both the dry and wet periods, groundwater flow is rapid along preferred pathways (karst and fault-based conduit network).

causing the increase in groundwater flow and storage of groundwater in conduit network. This rapid groundwater flow, when it occurs, is detected as an increase in $GRACE_{TWS}$ over the Dakhla subbasin, whereas groundwater flow in the surrounding matrix is slow resulting in little change in matrix storage and is not responsible for the observed $GRACE_{TWS}$ variations in the Dakhla subbasin. We realize that none of the individual pieces of evidence presented in this study can, on its own, conclusively prove the validity of the advocated model, yet collectively they provide substantial evidence in support of the advocated model and merit additional investigations over aquifers of similar geologic and hydrogeologic settings worldwide.

Our findings, we believe, have significant implications for groundwater sustainability of the NSAS in general, and for the arid sectors of the aquifer in particular. The current perception of the aquifer as being formed entirely of non-renewable fossil water should be revisited, even in its arid sectors (Dakhla subbasin and Northern Kufra section).

It should be also noted that the rapid groundwater flow in response to climatic variability observed over the NSAS and detected from GRACE data could be common to many of the fossil aquifers worldwide and might offer a viable explanation for the reported modern contributions in many of the deep aquifers elsewhere. While we believe that the response of deep aquifers to climatic variations remains a relatively slow process that takes thousands to tens of thousands of years, there is apparently a much faster response in aquifers that are characterized by dense networks of faults, fractures and karst as is the case with the NSAS. Examples of potential fossil aquifers which could be investigated for a similar rapid response to climate variability include the Saharan aquifer systems in North Africa and in the Arabian Peninsula. The largest of those aquifers is the Mega Aquifer System (area: 2×10^6 km^2; countries: Saudi Arabia, Oman, United Emirates, and Jordan) and the North Western Saharan Aquifer System (area: 1.2×10^6 km^2; countries: Algeria, Tunisia, and Libya). Additional smaller ($<900 \times 10^3$ km^2) Saharan aquifers include the Iullemeden Aquifer in Mali, Niger, Nigeria, Algeria and Benin and the Taoudeni Aquifer in Mauritania, Mali and Burkina Faso (Abotalib et al., 2016; Othman et al., 2018).

Acknowledgments

Funding was provided by National Aeronautics and Space Administration (NASA) Earth Science Division grants NNX12AJ94G and 80NSSC18K1681 and by the U.S.–Egypt Science and Technology (S&T) Joint Fund, administered by the National Academies of Sciences grant 2000007141 awarded to Western Michigan University, the Egyptian Ministry of Higher Education and Scientific Research, and the Earth Sciences Remote Sensing Facility at Western Michigan University. The opinions, findings, conclusions, or recommendations expressed in this article are those of the authors alone.

References

A, G., Wahr, J., Zhong, S., 2013. Computations of the viscoelastic response of a 3-D compressible Earth to surface loading: an application to Glacial Isostatic Adjustment in Antarctica and Canada. Geophys. J. Int. 192, 557–572. https://doi.org/10.1093/gji/ggs030.

Abotalib, A.Z., Sultan, M., Elkadiri, R., 2016. Groundwater processes in Saharan Africa: Implications for landscape evolution in arid environments. Earth-Science Rev https://doi.org/10.1016/j.earscirev.2016.03.004.

Abotalib, A.Z., Sultan, M., Jimenez, G., Crossey, L., Karlstrom, K., Forman, S., Krishnamurthy, R.V., Elkadiri, R., Polyak, V., 2019. Complexity of Saharan paleoclimate reconstruction and implications for modern human migration. Earth Planet. Sci. Lett. 508, 74–84. https://doi.org/10.1016/J.EPSL.2018.12.015.

Abouelmagd, A., Sultan, M., Sturchio, N.C., Soliman, F., Rashed, M., Ahmed, M., Kehew, A.E., Milewski, A., Chouinard, K., 2014. Paleoclimate record in the Nubian Sandstone Aquifer, Sinai Peninsula, Egypt. https://doi.org/10.1016/j.yqres.2013.10.017.

Ahmed, M., Abdelmohsen, K., 2018. Quantifying modern recharge and depletion rates of the Nubian Aquifer in Egypt. Surv. Geophys. 39, 729–751. https://doi.org/10.1007/s10712-018-9465-3.

Ahmed, M., Sultan, M., Wahr, J., Yan, E., 2014. The use of GRACE data to monitor natural and anthropogenic induced variations in water availability across Africa. Earth-Science Rev https://doi.org/10.1016/j.earscirev.2014.05.009.

Ahmed, M., Sultan, M., Yan, E., Wahr, J., 2016. Assessing and improving land surface model outputs over Africa using GRACE, field, and remote sensing data. Surv. Geophys. 37, 529–556. https://doi.org/10.1007/s10712-016-9360-8.

Alfaran, S.M.M.A., 2013. Geologic and geomorphologic impacts on the water resources, Tushka area and its vicinities, South Western Desert, Egypt. Doctoral thesis. Ain Shams University.

Aly, A.M., Froehlich, K., Nada, A., Awad, M., Hamza, M., Salem, W.M., 1993. Study of environmental isotope distribution in the Aswan High Dam Lake (Egypt) for estimation of evaporation of lake water and its recharge to adjacent groundwater. Environ. Geochem. Health 15, 37–49.

Andersen, T., Carstensen, J., Hernández-García, E., Duarte, C.M., 2009. Ecological thresholds and regime shifts: approaches to identification. Trends Ecol. Evol. 24, 49–57. https://doi.org/10.1016/J.TREE.2008.07.014.

Aref, E.M.M., Kadrah, A.M., Lotfy, Z.H., 1987. Karst topography and karstification processes in the Eocene limestone plateau of El Bahariya. Z. Geomorphol. N.F 31, 45–64.

Bakhbakhi, M., 2006. Nubian Sandstone Aquifer System. In: Foster, S., Loucks, D.P. (Eds.), Non-renewable Groundwater Resources: A Guidebook on Socially Sustainable Management for Water-policy Makers. United Nations Educational, Scientific and Cultural Organization, Paris, pp. 75–81.

Ball, J., 1927. Problems of the Libyan desert. Geogr. J. 70 (21-38,105-128,209-224).

Banks, D., Davies, C., Davies, W., 1995. The chalk as a karstic aquifer: evidence from a tracer test at Stanford Dingley, Berkshire, UK. Q. J. Eng. Geol. Hydrogeol. 28, S31–S38. https://doi.org/10.1144/GSL.QJEGH.1995.028.S1.03.

Bear, J., 1972. Dynamics of fluids in porous media. Elsevier, New York https://doi.org/10.1016/S0006-3223(98)00224-8.

Butzer, K.W., 1965. Desert landforms at the Kurkur Oasis. Egypt. Association Am. Geogr. 55, 578–591.

Chen, Z., Grasby, S.E., Osadetz, K.G., 2004. Relation between climate variability and groundwater levels in the upper carbonate aquifer, southern Manitoba, Canada. J. Hydrol. 290, 43–62. https://doi.org/10.1016/J.JHYDROL.2003.11.029.

Cheng, M., Ries, J.C., Tapley, B.D., 2011. Variations of the Earth's figure axis from satellite laser ranging and GRACE. J. Geophys. Res. 116, B01409. https://doi.org/10.1029/2010JB000850.

Conco, C., 1987. Geological Map of Egypt, Scale 1:500,000. Geological Survey and Egyptian General Petroleum Corporation, Cairo, Egypt.

Coplen, T.B., 1996. New guidelines for reporting stable hydrogen, carbon, and oxygen isotope-ratio data. Geochim. Cosmochim. Acta 60, 3359–3360. https://doi.org/10.1016/0016-7037(96)00263-3.

Craig, H., 1961. Isotopic variations in meteoric waters. Science 133, 1702–1703. https://doi.org/10.1126/science.133.3465.1702.

Dickinson, J., Ferré, T., Bakker, M., Crompton, B., 2014. A screening tool for delineating subregions of steady recharge within groundwater models. Vadose Zo. J. 13. https://doi.org/10.2136/vzj2013.10.0184.

Dietzel, M., Leis, A., Abdalla, R., Savarino, J., Morin, S., Böttcher, M.E., Köhler, S., 2014. 17O excess traces atmospheric nitrate in paleo-groundwater of the Saharan desert. Biogeosciences 11, 3149–3161. https://doi.org/10.5194/bg-11-3149-2014.

El Gammal, E., 2010. New Findings On The Karst In Nubia Sandstone Southern Egypt. Nat. Sci. 8, 125–129.

El-Hinnawi, M., Philibbos, E., Riad, S., El-Khawaga, M.M., 2005. Geological Map of the South Western Desert, Egypt. 30 Sheets, Scale 1:250,000.

El-Hinnawi, M., Philibbos, E., Riad, S., El-Khawaga, M.M., 2006. Geological Map of the North Western Desert, Egypt. 25 Sheets, Scale 1:250,000.

Elsaka, B., Alothman, A., Godah, W., 2016. On the contribution of GOCE satellite-based GGMs to improve GNSS/leveling geoid heights determination in Saudi Arabia. IEEE J. Sel. Top. Appl. Earth Obs. Remote Sens. 9, 5842–5850. https://doi.org/10.1109/JSTARS.2015.2495193.

Fairhead, J.D., Salem, A., Cascone, L., Hammill, M., Masterton, S., Samson, E., 2011. New developments of the magnetic tilt-depth method to improve structural mapping of sedimentary basins. Geophys. Prospect. 59, 1072–1086. https://doi.org/10.1111/j.1365-2478.2011.01001.x.

Fendorf, S., Michael, H.A., van Geen, A., 2010. Spatial and temporal variations of groundwater arsenic in South and Southeast Asia. Science 328, 1123–1127. https://doi.org/10.1126/science.1172974.

Geyer, T., Birk, S., Liedl, R., Sauter, M., 2008. Quantification of temporal distribution of recharge in karst systems from spring hydrographs. J. Hydrol. 348, 452–463. https://doi.org/10.1016/J.JHYDROL.2007.10.015.
Goode, D.J., 1996. Direct simulation of groundwater age. Water Resour. Res. 32, 289–296.
GRAS, 1988. Geological Research Authority of the Sudan, Khartoum. Geological Map of the Sudan, Scale 1: 1,000,000, Sheets 1 and 2. Robertson Research.
Halliday, W.R., 2003. Caves and karsts of northeast Africa. Int. J. Speleol. 32, 19–32. https://doi.org/10.5038/1827-806X.32.1.2.
Hanson, R.T., Dettinger, M.D., Newhouse, M.W., 2006. Relations between climatic variability and hydrologic time series from four alluvial basins across the southwestern United States. Hydrogeol. J. 14, 1122–1146. https://doi.org/10.1007/s10040-006-0067-7.
Healy, R.W., Cook, P.G., 2002. Using groundwater levels to estimate recharge. Hydrogeol. J. 10, 91–109. https://doi.org/10.1007/s10040-001-0178-0.
Hermina, M., 1990. The surroundings of Kharga, Dakhla and Farafra oases. The Geology of Egypt. Balkema, Rotterdam.
Hesse, K.H., Hissese, A., Kheir, O., Schnacker, E., Schneider, M., Thorweihe, U., 1987. Hydrogeological investigations in the Nubian Aquifer system, Eastern Sahara. In: Kilitzsch, E., Schranck, E. (Eds.), Research in Egypt and Sudan. Dietrich Reimer, Berlin, pp. 397–464.
Huffman, G.J., Bolvin, D.T., Nelkin, E.J., Wolff, D.B., Adler, R.F., Gu, G., Hong, Y., Bowman, K.P., Stocker, E.F., 2007. The TRMM multisatellite precipitation analysis (TMPA): Quasi-global, multiyear, combined-sensor precipitation estimates at fine scales. J. Hydrometeorol. 8, 38–55. https://doi.org/10.1175/JHM560.1.
Jasechko, S., Perrone, D., Befus, K.M., Bayani Cardenas, M., Ferguson, G., Gleeson, T., Luijendijk, E., McDonnell, J.J., Taylor, R.G., Wada, Y., Kirchner, J.W., 2017. Global aquifers dominated by fossil groundwaters but wells vulnerable to modern contamination. Nat. Geosci. 10, 425–429. https://doi.org/10.1038/ngeo2943.
Joseph, A., Frangi, J.P., Aranyossy, J.F., 1992. Isotope characteristics of meteoric water and groundwater in the Sahelo-Sudanese zone. J. Geophys. Res. 97, 7543. https://doi.org/10.1029/92JD00288.
Kerr, Y.H., Waldteufel, P., Wigneron, J.-P., Martinuzzi, J., Font, J., Berger, M., 2001. Soil moisture retrieval from space: the Soil Moisture and Ocean Salinity (SMOS) mission. IEEE Trans. Geosci. Remote Sens. 39, 1729–1735. https://doi.org/10.1109/36.942551.
Khan, S.D., Fathy, M.S., Abdelazeem, M., 2014. Remote sensing and geophysical investigations of Moghra Lake in the Qattara Depression, Western Desert, Egypt. Geomorphology 207, 10–22. https://doi.org/10.1016/J.GEOMORPH.2013.10.023.
Kohl, T., Evans, K.F., Hopkirk, R.J., Jung, R., Rybach, L., 1997. Observation and simulation of non-Darcian flow transients in fractured rock. Water Resour. Res. 33, 407–418. https://doi.org/10.1029/96WR03495.
Landerer, F.W., Swenson, S.C., 2012. Accuracy of scaled GRACE terrestrial water storage estimates. Water Resour. Res. 48. https://doi.org/10.1029/2011WR011453.
Lapcevic, P.A., Novakowski, K.S., Sudicky, E.A., 1999. The interpretation of a tracer experiment conducted in a single fracture under conditions of natural groundwater flow. Water Resour. Res. 35, 2301–2312. https://doi.org/10.1029/1999WR900143.
Long, D., Longuevergne, L., Scanlon, B.R., 2015. Global analysis of approaches for deriving total water storage changes from GRACE satellites. Water Resour. Res. 51, 2574–2594. https://doi.org/10.1002/2014WR016853.
Milewski, A., Sultan, M., Yan, E., Becker, R., Abdeldayem, A., Soliman, F., Gelil, K.A., 2009. A remote sensing solution for estimating runoff and recharge in arid environments. J. Hydrol. 373, 1–14. https://doi.org/10.1016/j.jhydrol.2009.04.002.
Miller, H.G., Singh, V., 1994. Potential field tilt—a new concept for location of potential field sources. J. Appl. Geophys. 32, 213–217. https://doi.org/10.1016/0926-9851(94)90022-1.
Mohamed, A., Sultan, M., Ahmed, M., Yan, E., Ahmed, E., 2017. Aquifer recharge, depletion, and connectivity: inferences from GRACE, land surface models, and geochemical and geophysical data. Bull. Geol. Soc. Am. https://doi.org/10.1130/B31460.1.
Mostafa, A., 2013. Paleokarst shafts in the western desert of Egypt: a unique landscape. Acta Carsologica 42. https://doi.org/10.3986/ac.v42i1.631.
Neev, D., 1975. Tectonic evolution of the Middle East and the Levantine basin (easternmost Mediterranean). Geology 3, 683. https://doi.org/10.1130/0091-7613(1975)3<683:TEOTME>2.0.CO;2.
Neev, D., Hall, J.K., Saul, J.M., 1982. The Pelusium Megashear System across Africa and associated lineament swarms. J. Geophys. Res. Solid Earth 87, 1015–1030. https://doi.org/10.1029/JB087iB02p01015.
Oruc, B., 2010. Edge detection and depth estimation using a tilt angle map from gravity gradient data of the Kozaklı-Central Anatolia region, Turkey. Pure Appl. Geophys. 168, 1769–1780. https://doi.org/10.1007/s00024-010-0211-0.
Othman, A., Sultan, M., Becker, R., Alsefry, S., Alharbi, T., Gebremichael, E., Alharbi, H., Abdelmohsen, K., 2018. Use of geophysical and remote sensing data for assessment of aquifer depletion and related land deformation. Surv. Geophys. 39, 543–566. https://doi.org/10.1007/s10712-017-9458-7.
Patterson, L.J., Sturchio, N.C., Kennedy, B.M., Van Soest, M.C., Sultan, M., Lu, Z.T., Lehmann, B., Purtschert, R., Alfy, Z. El, Kaliouby, B. El, Dawood, Y., Abdallah, A., 2005. Cosmogenic, radiogenic, and stable isotopic constraints on groundwater residence time in the Nubian Aquifer, Western Desert of Egypt. Geochemistry, Geophys. Geosystems 6. https://doi.org/10.1029/2004GC000779.
Prell, W.L., Kutzbach, J.E., 1987. Monsoon variability over the past 150,000 years. J. Geophys. Res. 92, 8411–8425. https://doi.org/10.1029/JD092iD07p08411.
Qian, J., Zhan, H., Zhao, W., Sun, F., 2005. Experimental study of turbulent unconfined groundwater flow in a single fracture. J. Hydrol. 311, 134–142. https://doi.org/10.1016/J.JHYDROL.2005.01.013.
Reeves, J., Chen, J., Wang, X.L., Lund, R., Lu, Q.Q., Reeves, J., Chen, J., Wang, X.L., Lund, R., Lu, Q.Q., 2007. A review and comparison of changepoint detection techniques for climate data. J. Appl. Meteorol. Climatol. 46, 900–915. https://doi.org/10.1175/JAM2493.1.
Rodell, M., Famiglietti, J.S., Wiese, D.N., Reager, J.T., Beaudoing, H.K., Landerer, F.W., Lo, M.-H., 2018. Emerging trends in global freshwater availability. Nature https://doi.org/10.1038/s41586-018-0123-1.
Rodionov, S.N., 2004. A sequential algorithm for testing climate regime shifts. Geophys. Res. Lett. 31. https://doi.org/10.1029/2004GL019448 n/a-n/a.
Ruggieri, R., 2001. Speleologia d'Egitto. Speleologia, Soc. Spel. Ital. Bol. 45, 42–51.
Russo, T.A., Lall, U., 2017. Depletion and response of deep groundwater to climate-induced pumping variability. Nat. Geosci. 10, 105–108. https://doi.org/10.1038/ngeo2883.
Sanford, K.S., 1935. Sources of water in the North-Western Sudan. Geogr. J. 85, 412–431.
Sarnthein, M., Tetzlaff, G., Koopman, B., Wolter, K., Pflaumann, U., 1981. Glacial and interglacial wind regimes over the eastern subtropical Atlantic and North-West Africa. Nature 293, 193–196.
Save, H., Bettadpur, S., Tapley, B.D., 2012. Reducing errors in the GRACE gravity solutions using regularization. J. Geod. 86, 695–711. https://doi.org/10.1007/s00190-012-0548-5.
Save, H., Bettadpur, S., Tapley, B.D., 2016. High-resolution CSR GRACE RL05 mascons. J. Geophys. Res. Solid Earth 121, 7547–7569. https://doi.org/10.1002/2016JB013007.
Scanlon, B.R., Zhang, Z., Save, H., Wiese, D.N., Landerer, F.W., Long, D., Longuevergne, L., Chen, J., 2016. Global evaluation of new GRACE mascon products for hydrologic applications. Water Resour. Res. 52, 9412–9429. https://doi.org/10.1002/2016WR019494.
Scanlon, B.R., Zhang, Z., Save, H., Sun, A.Y., Schmied, H.M., Van Beek, P.H., Wiese, D.N., Wada, Y., Long, D., Reedy, R.C., Longuevergne, L., Döll, P., Bierkens, M.F.P., 2018. Global Models Underestimate Large Decadal Declining and Rising Water Storage Trends Relative to GRACE Satellite Data. https://doi.org/10.1073/pnas.1704665115.
Seaton, W.J., Burbey, T.J., 2005. Influence of ancient thrust faults on the hydrogeology of the blue ridge province. Ground Water 43, 301–313. https://doi.org/10.1111/j.1745-6584.2005.0026.x.
Sturchio, N.C., Du, X., Purtschert, R., Lehmann, B.E., Sultan, M., Patterson, L.J., Lu, Z.-T., Müller, P., Bigler, T., Bailey, K., O'Connor, T.P., Young, L., Lorenzo, R., Becker, R., El Alfy, Z., El Kaliouby, B., Dawood, Y., Abdallah, A.M.A., 2004. One million year old groundwater in the Sahara revealed by krypton-81 and chlorine-36. Geophys. Res. Lett. 31, 2–5. https://doi.org/10.1029/2003GL019234.
Sultan, M., Sturchio, N., Hassan, F.A., Hamdan, M.A.R., Mahmood, A.M., ElAlfy, Z., Stein, T., 1997. Precipitation source inferred from stable isotopic composition of Pleistocene groundwater and carbonate deposits in the Western Desert of Egypt. Quat. Res. 48, 29–37. https://doi.org/10.1006/qres.1997.1907.
Sultan, M., Wagdy, A., Manocho, N., Sauck, W., Abdel Gelil, K., Youssef, A.F., Becker, R., Milewski, A., El Alfy, Z., Jones, C., 2007a. An integrated approach for identifying aquifers in transcurrent fault systems: The Najd shear system of the Arabian Nubian shield. J. Hydrol. 349, 475–488. https://doi.org/10.1016/j.jhydrol.2007.11.029.
Sultan, M., Yan, E., Sturchio, N., Wagdy, A., Milewski, A., Abdel Gelil, K., Manocha, N., Becker, R., 2007b. Natural discharge: a key to sustainable utilization of fossil groundwater. J. Hydrol. 335, 25–36. https://doi.org/10.1016/j.jhydrol.2006.10.034.
Sultan, M., Ahmed, M., Sturchio, N., Yan, Y.E., Milewski, A., Becker, R., Wahr, J., Becker, D., Chouinard, K., 2013. Assessment of the vulnerabilities of the Nubian Sandstone Fossil Aquifer, North Africa. In: Pielke, R.A. (Ed.), Climate Vulnerability. Elsevier, Cambridge, Massachusetts, pp. 311–333 https://doi.org/10.1016/B978-0-12-384703-4.00531-1.
Sultan, M., Ahmed, M., Wahr, J., Yan, E., Emil, M.K., 2014. Monitoring aquifer depletion from space. In: Lakshmi, V., Alsdorf, D., Anderson, M., Biancamaria, S., Cosh, M., Entin, J., Huffman, G., Kustas, W., Oevelen, P.V., Painter, T., Parajka, J., Rodell, M., Rüdiger, C. (Eds.), Remote Sensing of the Terrestrial Water Cycle. John Wiley {&} Sons, Inc, Hoboken, NJ, pp. 347–366 https://doi.org/10.1002/9781118872086.ch21.
Swenson, S., Wahr, J., 2006. Post-processing removal of correlated errors in GRACE data. Geophys. Res. Lett. 33.
Swenson, S., Chambers, D., Wahr, J., 2008. Estimating geocenter variations from a combination of GRACE and ocean model output. J. Geophys. Res. Solid Earth 113. https://doi.org/10.1029/2007JB005338.
Tapley, B.D., Bettadpur, S., Ries, J.C., Thompson, P.F., Watkins, M.M., 2004a. GRACE measurements of mass variability in the Earth system. Science 305 (5683), 503–505. https://doi.org/10.1126/science.1099192.
Tapley, B.D., Bettadpur, S., Watkins, M., Reigber, C., 2004b. The gravity recovery and climate experiment: mission overview and early results. Geophys. Res. Lett. 31, L09607. https://doi.org/10.1029/2004GL019920.
Thorweihe, U., 1986. Isotopic identification and mass balance of the Nubian Aquifer System in Egypt. In: Thorweihe, U. (Ed.), Impact of climatic variations on East Saharian groundwaters—modelling of large scale flow regimes, Proceedings of a Workshop on Hydrology. ser. A 72. Berliner Geowissenschaftliche Abhandlungen, Berlin, pp. 87–97.
Thurmond, A.K., Stern, R.J., Abdelsalam, M.G., Nielsen, K.C., Abdeen, M.M., Hinz, E., 2004. The Nubian Swell. https://doi.org/10.1016/j.jafrearsci.2004.07.027.
Verduzco, B., Fairhead, J.D., Green, C.M., Mackenzie, C., 2004. New ınsights into magnetic derivatives for structural mapping, Lead. Lead. Edge 23, 116–119.
Villarini, G., Serinaldi, F., Smith, J.A., Krajewski, W.F., 2009. On the stationarity of annual flood peaks in the continental United States during the 20th century. Water Resour. Res. 45. https://doi.org/10.1029/2008WR007645.
Wahr, J., Molenaar, M., Bryan, F., 1998. Time variability of the Earth's gravity field: Hydrological and oceanic effects and their possible detection using GRACE. J. Geophys. Res. 103, 30205–30229.
Wahr, J., Swenson, S., Zlotnicki, V., Velicogna, I., 2004. Time-variable gravity from GRACE: First results. Geophys. Res. Lett. 31.

Waltham, T., 2001. Pinnacles and barchans in the Egyptian desert. Geol. Today 17, 101–104. https://doi.org/10.1046/j.0266-6979.2001.00288.x.
Walton, W.C., 2011. Aquifer system response time and groundwater supply management. Ground Water 49, 126–127. https://doi.org/10.1111/j.1745-6584.2010.00770.x.
Watkins, M.M., Wiese, D.N., Yuan, D.N., Boening, C., Landerer, F.W., 2015. Improved methods for observing Earth's time variable mass distribution with GRACE using spherical cap mascons. J. Geophys. Res. B Solid Earth 120, 2648–2671. https://doi.org/10.1002/2014JB011547.
Wouters, B., Bonin, J.A., Chambers, D.P., Riva, R.E.M., Sasgen, I., Wahr, J., 2014. GRACE, time-varying gravity, Earth system dynamics and climate change. Reports Prog. Phys. 77. https://doi.org/10.1088/0034 -4885/77/11/116801.
Yan, Z.W., Petit-Maire, N., 1994. The last 140-Ka in the Afro-Asian arid/semi-arid transitional zone. Palaeogeogr. Palaeoclimatol. Palaeoecol. 110, 217–233. https://doi.org/10.1016/0031-0182(94)90085-X.